Analysis and Optimisation of Quantum Cascade Structures

Martin Lindskog
Master Thesis
Supervisor: Prof. Andreas Wacker
Division of Mathematical Physics, Lund University

May 22, 2012

Abstract

The quantum cascade laser (QCL) is a semiconductor heterostructure using inter sub-band transitions to generate stimulated emission. The quantum cascade detector (QCD) is a similar to the QCL, but the heterostructure is tailored to absorb radiation and give a read-out current. In this work, three planned or realised QCL:s and two QCD:s have been simulated and analysed using a program based on the non-equilibrium Green's function theory technique (NEGFT) and comparing to experimental measurements. The importance of electron-electron scattering for thermalisation has been phenomenologically studied by altering the barrier deformation potential and a planned QCL has been optimised to give twice the gain from the original structure. The work has involved corporations with experimental groups at the National Research Council in Ottawa and the University of Waterloo, Canada, which resulted in an article published in the Journal of Applied Physics[1].

A new way to display the global behaviour of a QCL in terms of carrier concentration and density of states, by using the spectral function has been developed. For the first time, a QCD has been simulated by NEGFT to give space- and energy-resolved carrier concentrations, density of states and energies of the electronic states.

The agreement of NEGFT simulations to experiment is also analysed. The model applies very well to many structures, but the lack of electron-electron interaction causes problems with thermalisation for some structures.

I thank my supervisor Prof. Andreas Wacker for his strong support through discussion, teaching and understanding. I also thank him for the contacts with different researchers around the world he has propagated to me. I thank David Winge for the valuable discussions we had together over the course of this work. I thank Frida Franckie for letting me work early and late, for understanding, supporting and showing interest for my progress. I thank my family for all the help, especially when we had to leave our home during the course of this project. I also want to thank the staff at the division of Mathematical Physics for the very friendly and inspiring athmosphere.

Martin Lindskog, 4th of May 2012, Lund

Contents

1 Introduction

Today, lasers are a natural part of our lives, and are vital in applications within science, medicine and technology. The quantum cascade laser (QCL) is a laser made from the conduction band of a semiconductor heterostructure, forming subsequent quantum wells. It allows for precise lasing wavelengths and it partly covers the difficult-to-reach THz range from 0.3-10 THz. The QCL has a wide range of applications, from atmospheric and space spectroscopy to thermal imaging to security scanning[5]. In recent years, infrared (IR) QCL:s have been introduced on the market, and recently Statoil bought a set of IR QCL:s in order to monitor waste water from their oil rigs[6].

The quantum cascade detector (QCD) is a recently developed device, similar to the quantum well infrared photodetector (QWIP), but has the advantage of being operated without an external bias, heavily suppressing leakage currents under dark conditions. The hope is for QCD:s to help in identifying molecular and atomic signals in gases. Important future applications are diagnostics from exhaled air in medicine, detection and limitation of leaking chemicals from industries in sensitive environments, as well as infrared imaging[7].

Motivation

The motivation of this work is to help progress toward high-temperature QCL:s and QCD:s by simulating and understanding current state-of-the-art lasers and detectors, their benefits and limitations. The goal is to be able to help in improving the performance of the devices.

The long-term goal of QCL research is developing applications in a variety of fields, ranging from diagnostics through exhaled air in medicine, to precise spectroscopic measurements in astrophysics. The potential benefit to society is great, once QCL:s can be commercially available as a table top device, which requires a much increased temperature performance.

QCD:s are important for detecting in the infrared, a region that is now dominated by quantum well infrared detectors (QWIP:s). These detectors suffer from several dis-benefits, however. QWIP:s are operated under an external bias and have the problem of currents even in completely dark conditions. The QCD requires no bias applied under operation, which reduces the dark current substantially (even though a very small bias can reduce the dark current even further). The purpose of these IR detectors is primarily thermal imaging. Contrary to THz QCL:s, QCD:s can be operated at room temperature due to the large energy separation between the ground state and the excitation states.

Quantum Cascade Lasers

The first quantum cascade laser (QCL) was realised in 1994[8], and it was a mid-infrared QCL. Infrared (IR) QCL:s have been dominating the field since, but are limited by the optical phonon frequency (typically 7-12 THz in semiconductor materials) and the resulting Reststrahlen band. The type of QCL focused on in this work is the THz QCL first realised in 2002[9], operating below the optical phonon frequency.

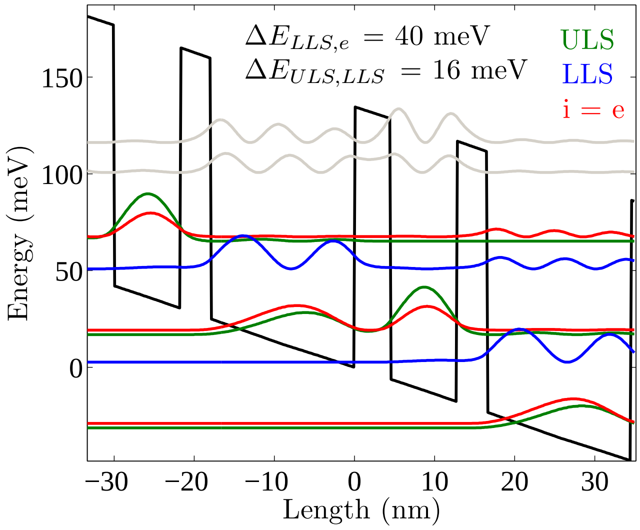

Figure 1: Conduction band edge and the Wannier-Stark states of the structure investigated in Ref. [2]. The different colours represent the lower laser state (LLS), upper laser state (ULS), the extraction (e) and injection (i) levels. The injection and extraction levels are the same in this particularly simple structure. The alignment between the injection level and the ULS provides efficient tunnelling realised tunnelling filling the ULS of the next period.

For many years it was thought impossible to construct a QCL that operated at a temperature higher than the lasing frequency, $k_B T < \hbar\omega$. The reason for this assessment was that the carriers would have enough thermal energy to counter-act the inversion process somehow. There is no physical foundation for such a rule, however, and many lasers have been built that overcome it. Now the quest is on for THz QCLs to reach ever higher operating temperatures. A THz QCL has yet to be proven to work above 200 K, the closest record published just a few months ago being 199.5 K[10]. The goal would be a working laser around $T = 250$ K, since then it would be possible to cool the device electronically by Peltier cooling e. g., which would allow for a table-top device rather than large tanks of liquid nitrogen to be re-filled and handled with. The two largest problems to be overcome is so-called thermal backfilling, where electrons might get thermally excited to e. g. the LLS from the extraction level and reduce invention, and acoustic phonon scattering, opening up additional current channels skipping the lasing transition.

The heterostructures are made by molecular beam epitaxy (MBE), a very lengthy process where one period of about 10 subsequent wells and barriers is repeated about 200 times for the ordinary THz QCL, which requires the operator to be present constantly for as long as 18 hours.

Quantum Cascade Detectors

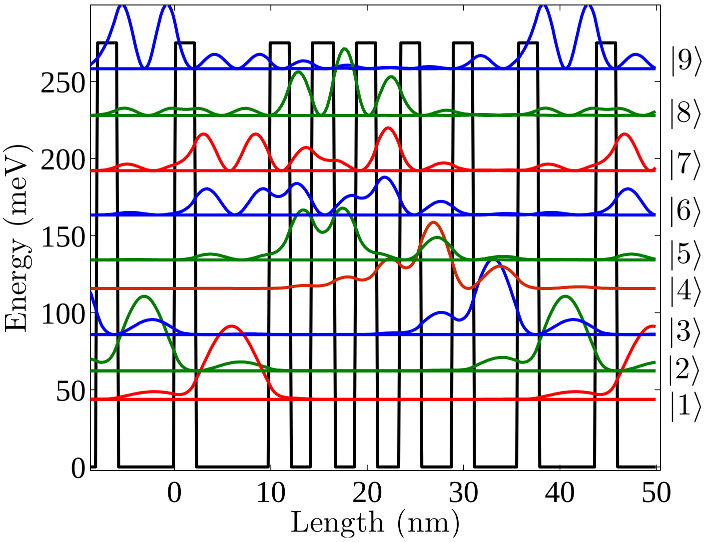

Figure 2: Conduction band profile and the quantum mechanical states of a QCD made by Ref. [3].

The first quantum cascade detector (QCD) was realized in 2004[3] and is constructed in a way similar to the QCL, see figure 1. The wells are tailored such that mainly a low-lying ground state $|1\rangle$ is populated with electrons. A photon of an energy matching a transition from the state $|1\rangle$ to a high-energy state in the same well (e. g. $|6\rangle$) puts an electron into this excited state. In the neighboring well, which is much more narrow, there is a state close in energy to the excited state in the first well, and the electron tunnels through and de-excites to a state of lower energy. It then tunnels and de-excites again and again in a cascade down to the ground state of the next period. When many electrons are excited, this induces a current to be detected at the leads of the heterostructure.

This design requires the ground state to overlap very little with the states leaking into the first well from the neighbouring wells, in order to get only one peak in the response spectrum. It is also necessary to have the state in the last well separated from the ground state energy enough to have only a small population, for the same reason. The importance of having only one peak is that we want to detect at one frequency. If we have several peaks we would detect at other frequencies as well, thus being unable to know at what frequency we are actually detecting.

Part I

Theory

2 Heterostructure

The concept of a QCL uses the idea of a quantum well, the popular example of illustrating quantum mechanics. One of the most common combination of materials used is GaAs in the well and $Al_xGa_{1-x}As$ in the barriers (x is the relative amount of aluminum to gallium) which are schematically drawn in figure 3. When put together, the conduction and valence band edges will bend at the interfaces, with a conduction band offset of typically 250-300 meV. The quantum cascade laser exploits inter sub-band transitions in the conduction band, where electrons are injected by adding donor atoms. The valence band is completely full, and so we fully turn our attention to what is happening in the conduction band from now on. In the z-direction (the growth direction), the electrons incoming from the left will see a barrier in the GaAs/AlGaAs conduction band offset. In the transverse directions (x and y), however, the electrons are not quantized and thus the elec-

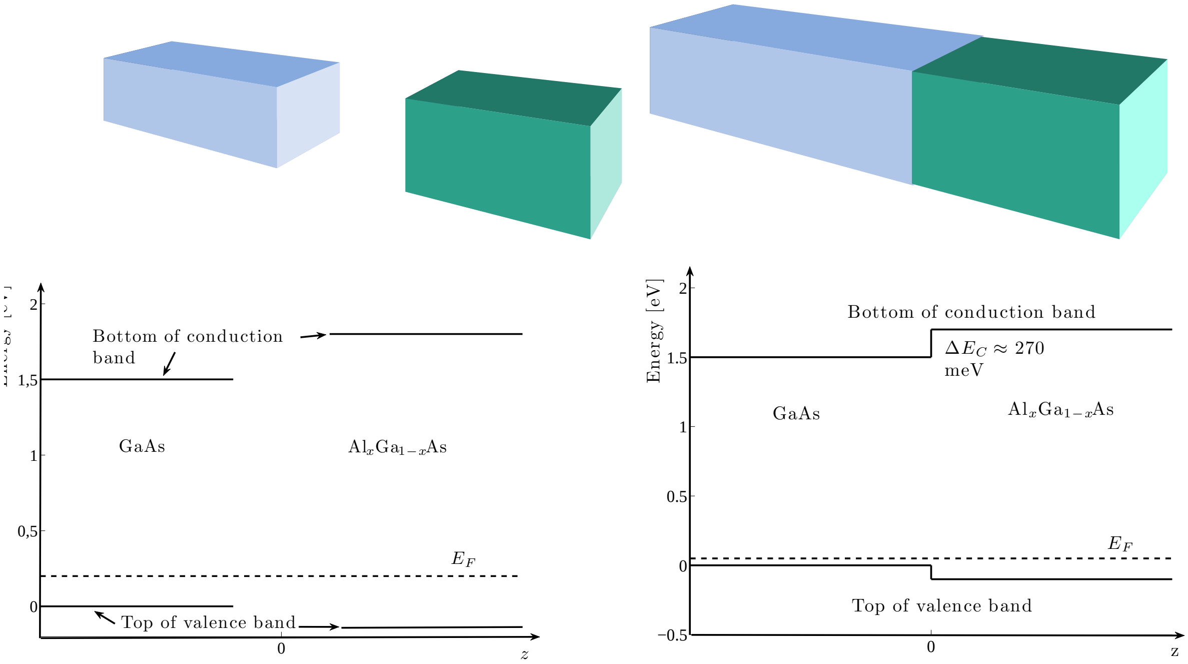

Figure 3: Two pieces of bulk GaAs and AlGaAs have different band structure and different band gaps at the Γ-point. Put together, the bands will bend at the interface between the materials.

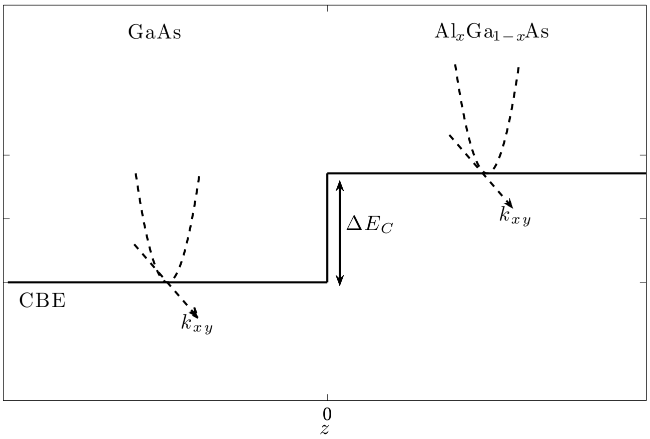

Figure 4: The conduction band profile of a simpel GaAs/AlGaAs heterostructure.

trons can have any energy E_k associated with the (transverse) crystal momentum k. This is depicted in figure 4

Quantum wells are made in the conduction band by alternating between thin layers of materials with different band gaps as in figure 5. The electronic wave-function is quantized according to the depth of the well and the widths of the wells and barriers. This allows for tailoring the energies and extensions of the quantum mechanical states and electronic wave-functions. When many quantum wells are placed in sequence, electrons can tunnel across the AlGaAs barriers to neighboring wells. When a bias is applied, see figure 6(a), the whole band structure bends in energy and the tunneling electrons will constitute a tunneling current. For the structure in figure 6(a), the current as a function of applied bias is shown in figure 6(b).

The idea of a quantum cascade laser is now to tailor the quantum wells and barriers, so that an applied bias will drive the electronic current in such a way that inversion is created between two sub-bands. When inversion is present, electrons from the upper laser level (with higher electron density) can be de-excited by stimulated emission into the lower laser state (with less electron density).By manipulating the wells, we can get any suitable separation in energy between the states. The energy difference between the lower laser state and some extraction state, e. g., is preferably tuned to the optical phonon energy to get an efficient scattering rate. Alternatively, the two states are tuned into resonance to get an efficient tunnelling rate in order to maintain inversion.

One such tailored structure is shown in figure 1, where the short-hand notation for the lower laser state (LLS), upper laser state (ULS), extraction level (e) and injection level (i) has been introduced. This is actually the simplest structure

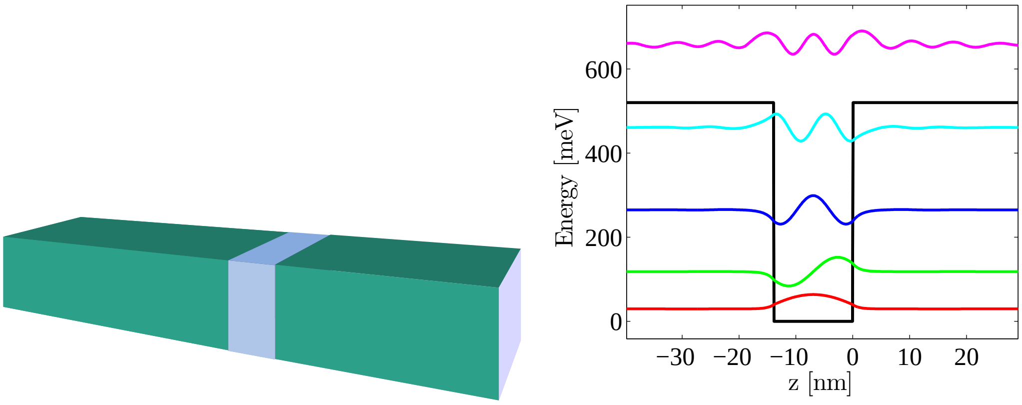

Figure 5: Slicing a thin slab of GaAs inside a AlGaAs slab creates a quantum well confinement potential for the electrons in the conduction band.

possible[11], with only three active states and two wells per period. This strucutre is a working QCL that is examined later in this work.

This is how the laser scheme works: the electrons can be de-excited from a state of higher energy (ULS) to a state of lower energy (LLS) by stimulated emission, when a photon with the energy of the level separation interacts with the electrons. For this to work, inversion is necessary, i. e. more carriers have to be in the ULS than in the LLS. The inversion is driven by the bias voltage, transporting the carriers from the LLS to the ULS in the next period. Efficient tunnelling and phonon driven scattering mechanisms also aid the carriers to reach inversion.

3 Model

The properties of a quantum cascade laser are quantum mechanical in nature, and since we are dealing with many (10^{10}) particles we need some kind of theory for treating many-body quantum systems. The simplest approach would be using quantum rate equations, but this has proved not to be reliable in all cases. Another common approach is the density matrix theory, in which one characterises a quantum state by its density matrix describing the overlap between the basis states

$$\rho_{ij} = \langle \Psi_i | \hat{\rho} | \Psi_j \rangle = \mathrm{Tr}\{\hat{\rho} a_j^\dagger a_i\}, \tag{1}$$

where $\hat{\rho}$ is the density operator. This method, being relatively easy to understand and giving fast calculations, is also not completely reliable.

For the above reasons, the method used for the calculations in this work is the non-equilibrium Green's function theory (NEGFT). It revolves around the rather abstract definition of the Green's function (related to a propagator) of the quantum system, from which the observables of interest can be derived. The theory is

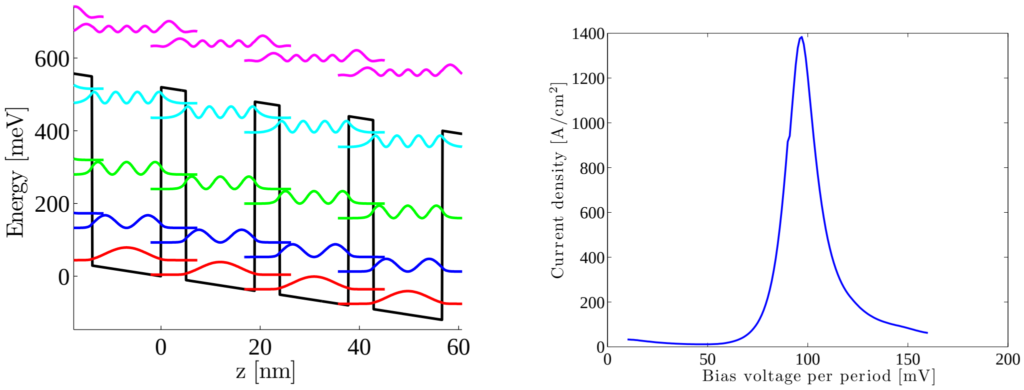

(a)

(b)

Figure 6: (a): Superlattice structure with an applied bias of 40 mV per period. (b): Current vs. applied bias per period. A peak occurs at around 100 mV/period, where the ground state of one well aligns with the first excited state of the neighboring well down stream.

rather complicated and non-intuitive at first glance, but has proved to give very accurate results in most cases. As will be seen in this work, the NEGFT allows us to calculate currents quantitatively and gain spectra qualitatively. The gain calculation has not been tested sufficiently for its quantitative value for predicting laser outputs due to the complications of losses in the waveguides used in the real case. Qualitatively, it seems to be able to reproduce experimental data well in most cases.

The periodicity of the hetero-structure implies Bloch functions are good quantum states. However, they are extending over the entire structure by definition and we need to think of localised states extending over one period at most, to be able to predict electron distributions and currents. We therefore use the Wannier states, which are superpositions of Bloch states, with a phase chosen in a clever way to maximally localise the states.

The basis states of the calculations will be discussed in the first section of the theory part, mostly inspired by Ref. [12]. The Green's function theory follows next, mainly taken from Refs. [12], [13] and [14]. The structure of the Hamiltonian also needs some discussion. We end the theoretical part of this work with a description of how the current and gain are calculated.

The program has been developed and tested by my supervisor, prof. Andreas Wacker with colleagues, during the course of many years. In order to to get a feeling of where the results come from and what is needed as inputs to the program, this part of the thesis will discuss the theory behind the program.

The following discussion is rather technical and describes the method used in the implementation of the program. However, if the reader is primarily interested in the results and analysis of the quantum cascade structures, they may skip directly to part II since the theory in full detail is not vital to appreciate the results and their implications.

4 Basis States

The quantum cascade laser and detector is built up from layers of alternating material, to form quantum wells and barriers in the conduction band. Figure 1 shows the conduction band edge and the Wannier-Stark states at a certain bias. The structure is periodic (in the figure, one period is 34.5 nm long), with on the order of 10 layers of different thickness in each period. For THz lasers, the period is repeated on the order of 200-300 times[2][1], and for IR lasers it is much less, typically in the order of 10 times[15].

The periodicity of the structure implies that Bloch functions are a good choice of basis states, however they are non-local and are thus not suited to describe the dynamics within a single period. For this reason, the basis states used for the calculations are the so-called Wannier states, defined by

$$\psi_{\mathbf{R}}^{\nu}(\mathbf{r}) = \frac{1}{\sqrt{N}} \sum_{\mathbf{k}} e^{-i\mathbf{k}\mathbf{R}} \varphi_{\mathbf{k}}^{\nu}(\mathbf{r}) \tag{2}$$

from the crystal Bloch functions

$$\varphi_{\mathbf{k}}^{\nu}(\mathbf{r}) = e^{i\mathbf{k}\cdot\mathbf{r}} u_{\mathbf{k}}^{\nu}(\mathbf{r}), \tag{3}$$

which are defined up to an arbitrary phase. $u_{\mathbf{k}}^{\nu}(\mathbf{r})$ has the periodicity of the heterostructure. The phase can be chosen so as to maximise the localisation of the Wannier states. $\mathbf{R}$ is any lattice vector, N is the number of unit cells in the crystal and ν is the subband index. The Wannier states constitutes an orthonormal basis. Using that the crystal is symmetric and homogeneous in the (x, y)-plane and periodic in the z-direction and replacing the sum with an integral, one can write

$$\psi^{\nu}(z - nd) = \frac{d}{2\pi} \int_{-\pi/d}^{\pi/d} dq e^{-inqd} \varphi_{q}^{\nu}(z). \tag{4}$$

4.1 Miniband Energy

For each layer of the superlattice, $z_j < z < z_{j+1}$, it is possible to construct an envelope function

$$f_j(z) = A_j e^{ik_j(E)(z-z_j)} + B_j e^{-ik_j(E)(z-z_j)} \tag{5}$$

satisfying the Schrödinger equation for the effective Hamiltonain. At the boundary between two layers j and $j+1$ (at $z=0$), the envelope functions of the respective layers must satisfy

$$\begin{aligned} f(\mathbf{r})|_{z\to 0^-} &= f(\mathbf{r})|_{z\to 0^+} && (6) \\ \frac{1}{m_j}\frac{\partial f(\mathbf{r})}{\partial z}|_{z\to 0^-} &= \frac{1}{m_{j+1}}\frac{\partial f(\mathbf{r})}{\partial z}|_{z\to 0^+}. && (7) \end{aligned}$$

This gives the set of equations for the coefficients A_i and B_i, on matrix form,

$$\begin{pmatrix} A_{j+1} \\ B_{j+1} \end{pmatrix} = M_j(E)\begin{pmatrix} A_j \\ B_j \end{pmatrix}, \tag{8}$$

with

$$M_j = \frac{1}{2}\begin{pmatrix} (1+\frac{k_j m_{j+1}}{k_{j+1}m_j})e^{ik_j(z_{j+1}-z_j)} & (1-\frac{k_j m_{j+1}}{k_{j+1}m_j})e^{-ik_j(z_{j+1}-z_j)} \\ (1-\frac{k_j m_{j+1}}{k_{j+1}m_j})e^{ik_j(z_{j+1}-z_j)} & (1+\frac{k_j m_{j+1}}{k_{j+1}m_j})e^{-ik_j(z_{j+1}-z_j)} \end{pmatrix}. \tag{9}$$

For a heterostructure with M layers, one can iterate (8) to yield

$$\begin{pmatrix} A_{M+1} \\ B_{M+1} \end{pmatrix} = \prod_{j=1}^{M} M_j(E)\begin{pmatrix} A_1 \\ B_1 \end{pmatrix} = e^{iqd}\begin{pmatrix} A_1 \\ B_1 \end{pmatrix}, \tag{10}$$

using the fact that the Bloch function satisfies $\varphi_q(z+d) = e^{iqd}\varphi_q(z)$.

The heterostructure has a period d, and the allowed values for q are therefore limited to the Brillouin zone $-\pi/d < q < \pi/d$, and $E^\nu(q+\pi/d) = E^\nu(q-\pi/d)$. This allows for Fourier expanding the dispersion $E^\nu(q)$ as

$$\begin{aligned} E^\nu(q) &= \frac{a_0^\nu}{2} + \sum_{h=1}^{\infty}\left[a_h^\nu \cos\left(h\frac{2\pi}{d}q\right) + b_h^\nu \sin\left(h\frac{2\pi}{d}q\right)\right] && (11) \\ a_h^\nu &= \frac{d}{\pi}\int_{-\pi/d}^{\pi/d} dq E^\nu(q)\cos(hdq) && (12) \\ b_h^\nu &= \frac{d}{\pi}\int_{-\pi/d}^{\pi/d} dq E^\nu(q)\sin(hdq) = 0 && (13) \end{aligned}$$

where (13) becomes zero since $E^\nu(q)\sin(hdq)$ is an odd function. From (12), for $h=0$ we get

$$\frac{a_0}{2} = \frac{d}{2\pi}\int_{-\pi/d}^{\pi/d} dq E^\nu(q) \equiv E^\nu, \tag{14}$$

where E^ν is defined as the center of the miniband. We can now write

$$E^\nu(q) = E^\nu + \sum_{h=1}^{\infty} 2T_h^\nu \cos(hdq), \tag{15}$$

where

$$T_h^\nu \equiv \frac{a_h^\nu}{2} = \frac{d}{2\pi}\int_{-\pi/d}^{\pi/d} E^\nu(q)\cos(hdq)dq. \tag{16}$$

$T_1^\nu >> T_{h\geq 2}^\nu$ in most cases and so neglecting higher orders in h is often appropriate. $E^\nu(q)$ are obtained by solving equation (10).

4.2 Second Quantization

The Hamiltonian is written in second quantization as

$$\hat{H} = \sum_\nu \int_{-\pi/d}^{\pi/d} dq E^\nu(q) a_q^{\nu\dagger} a_q^\nu \tag{17}$$

where a_q^ν is the annihilation and $a_q^{\nu\dagger}$ the creation operator, annihilating and creating an electron in the Bloch state in band ν with momentum q. The annihilation and creation operators in the Wannier basis are defined as

$$\begin{aligned} a_q^\nu &= \sqrt{\frac{d}{2\pi}}\sum_n e^{-iqnd} a_n^\nu && (18)\\ a_q^{\nu\dagger} &= \sqrt{\frac{d}{2\pi}}\sum_n e^{iqnd} a_n^{\nu\dagger}, && (19)\end{aligned}$$

which gives the Hamiltonian in the Wannier basis

$$\begin{aligned} \hat{H} &= \sum_\nu \int_{-\pi/d}^{\pi/d} dq \sum_{m,n} \Big[E^\nu \frac{d}{2\pi} e^{iqd(m-n)} a_m^{\nu\dagger} a_n^\nu \\ &\quad + \sum_{h=1}^{\infty} 2T_h^\nu \frac{e^{idq(m-n+h)} + e^{idq(m-n-h)}}{2} \frac{d}{2\pi} a_m^{\nu\dagger} a_n^\nu \Big] \\ &= \sum_{\nu,n} E^\nu a_n^{\nu\dagger} a_n^\nu + \sum_{h=1}^{\infty} T_h^\nu \left(a_n^{\nu\dagger} a_{n+h}^\nu + a_n^{\nu\dagger} a_{n-h}^\nu\right), \end{aligned} \tag{20}$$

where the cosine in (15) has been expanded using Euler's formula. Heisenberg's equation of motion gives the time dependence of the Heisenberg operator $a_n^\nu(t)$, neglecting terms with $h \geq 2$,

$$i\hbar \frac{\partial a_n^\nu(t)}{\partial t} = [\hat{H}, a_n^\nu(t)] = E^\nu a_n^\nu + T_1^\nu \left(a_{n-1}^\nu + a_{n+1}^\nu\right), \tag{21}$$

using the commutator identities

$$\begin{aligned} [a_{m+l}^{\nu\dagger} a_m^\nu, a_n^\nu] &= a_{m+l}^{\nu\dagger}[a_m^\nu, a_n^\nu] + [a_{m+l}^{\nu\dagger}, a_n^\nu] a_m^\nu = \\ &= a_{m+l}^{\nu\dagger}\{a_m^\nu, a_n^\nu\} - \{a_{m+l}^{\nu\dagger}, a_n^\nu\} a_m^\nu = \delta_{m+l,n}^{\mu,\nu} a_m^\mu \end{aligned} \tag{22}$$

and anti-commutation relations for the fermionic annihilation operator

$$\begin{aligned}\{a_m^{\mu}, a_n^{\nu}\} &= 0 && (23)\\ \{a_m^{\mu\dagger}, a_n^{\nu}\} &= \delta_{m,n}^{\mu,\nu}. && (24)\end{aligned}$$

4.3 Wannier-Stark Basis

Let us now add a constant electric field F, uniform over the entire heterostructure, giving rise to a potential energy

$$e\phi(z) = -eFz, \tag{25}$$

where $e < 0$ is the electron charge. This will change the Hamiltonian (20) to

$$\hat{H}_{nn'}^{\nu\nu'} \longrightarrow \hat{H}_{nn'}^{\nu\nu'}\delta_{\nu\nu'} - eFz_{nn'}^{\nu\nu'} \tag{26}$$

which is non-diagonal in the Wannier basis, and solving the Shrödinger equation for the Hamiltonian (26) gives the Wannier-Stark states $|\phi_j^{\nu}\rangle$ as the eigenstates. The Wannier-Stark states can be expanded in the Wannier basis, mixing the Wannier states due to the presence of an electric field. The Wannier-Stark states form a ladder in both space and energy with the same wavefunctions appearing each heterostructure period.

The Wannier-Stark states are not used in the actual calculations, but are a helpful tool for displaying, discussing and understanding a quantum cascade structure. In practice, they are also calculated with a mean field potential (described in more detail in section 6.1), and so they show more accurately what the eigenstates look like, than if one were to show the Wannier states.

5 Green's Functions

In the following, $\vec{x}$ and $\vec{k}$ stand for 3D quantities, $\mathbf{x}$ and $\mathbf{k}$ 2D quantities and 1D quantities or absolute values are written in italic face (x, k). The Green's functions of the system are defined by the correlation functions[13]

$$\begin{aligned}G_{\mu\nu,mn}^{<}(t,t') &= i\langle a_{\nu,n}^{\dagger}(t')a_{\mu,m}(t)\rangle && (27)\\ G_{\mu\nu,mn}^{>}(t,t') &= i\langle a_{\mu,m}(t)a_{\nu,n}^{\dagger}(t')\rangle && (28)\\ G_{\mu\nu,mn}^{R}(t,t') &= -i\theta(t-t')\langle\{a_{\mu,m}(t), a_{\nu,n}^{\dagger}(t')\}\rangle && (29)\\ G_{\mu\nu,mn}^{A}(t,t') &= i\theta(t'-t)\langle\{a_{\mu,m}(t), a_{\nu,n}^{\dagger}(t')\}\rangle, && (30)\end{aligned}$$

where the expectation value of an operator $\hat{A}$ is defined as $\langle\hat{A}\hat{\rho}\rangle$. The correlation functions (27)-(30) are matrices in the band μ,ν and period m,n indices. When convenient, these are contracted to $\alpha = \mu m$ and $\beta = \nu n$, or suppressed completely when they are superfluous. From this definition of the Green's functions, all relevant observables of the system can be obtained.

If the system has a Hamiltonian with a periodic time-dependence with period $T = 2\pi/\Omega$, we can define the Fourier transform of $G^<(t_1, t = t_2 - t_1)$ as[16]

$$G^<_h(E) \quad = \quad \frac{1}{\hbar}\int_{-\infty}^{\infty} dt \frac{1}{T}\int_0^T dt_1 e^{ih\Omega t_1} e^{iEt/\hbar} G^<(t_1, t_1 - t). \tag{31}$$

In the following the notation $E = \hbar\omega$ is used for the Fourier transform of the difference time. From the definitions of the Green's function and the correlation functions (27)-(30) all relevant observables can be obtained. For example, the density matrix is

$$\rho_{\alpha,\beta}(\mathbf{k}, t) = \langle \psi^\dagger_\beta(\mathbf{k}, t)\psi_\alpha(\mathbf{k}, t)\rangle = -i\sum_h \int \frac{dE}{2\pi} G^<_{\alpha\beta,h}(\mathbf{k}, E)e^{-ih\Omega t}. \tag{32}$$

The spectral function for stationary systems is defined as

$$A(\vec{k}, \omega) = i[G^R(\vec{k}, \omega) - G^A(\vec{k}, \omega)] = i[G^>(\vec{k}, \omega) - G^<(\vec{k}, \omega)] \tag{33}$$

and satisfies

$$\int \frac{d\omega}{2\pi} A(\vec{k}, \omega) \quad = \quad 1 \tag{34}$$

$$\int \frac{d^3k}{(2\pi)^3} A(\vec{k}, \omega) \quad = \quad \rho(\omega), \tag{35}$$

where $\rho(\omega)$ is the energy resolved density of states. It then follows that

$$G^<(\vec{k}, \omega) = if(\omega)A(\vec{k}, \omega) \tag{36}$$

in equilibrium, where

$$f(\omega) = \frac{1}{e^{(\omega-\mu)/k_B T} + 1} \tag{37}$$

is the Fermi distribution function.

5.1 Self-Energies

The full Green's function can be written as[14]

$$G(\vec{k}, E) = G_0(\vec{k}, E) + G_0(\vec{k}, E)\Sigma(\vec{k}, E)G(\vec{k}, E), \tag{38}$$

where $\Sigma(\vec{k}, E)$ is called the (proper) self-energy and is the sum of all irreducible Feynman diagrams. Equation (38) is called the Dyson equation and gives an iterative expression for the Green's function.

G_0 is the zeroth order term in the perturbation expansion of G, and is the free-particle Green's function. In Fourier space, $G_0(\vec{k}, E)$ can be written

$$G_0(\vec{k}, \omega) = \frac{1 - f_k}{\omega - \epsilon_k + i\eta} + \frac{f_k}{\omega - \epsilon_k - i\eta}, \tag{39}$$

where ϵ_k comes from the time-dependence of $a_k(t) = e^{-i\epsilon_k t} a_k(0)$. Σ can also be written in terms of G_0 and the matrix elements of the different interactions in the respective Feynman diagrams.

In the self-consistent Born approximation, the phonon-electron self-energies are approximated by[13]

$$\Sigma(k, E) = \frac{i}{\hbar} \sum_q \int \frac{dE'}{2\pi} M_q^2 G(k - q, E - E') D_0(q, E'), \tag{40}$$

where D_0 is the phonon Green's function and M_q the matrix element for the interaction with momentum q.

5.2 Non-Equilibrium

With a time-dependent Hamiltonian there is no guarantee for equilibrium and all observables have a complicated dependence on $H'(t)$. In order to simplify the matters, a contour integration along the Keldysh contour is inferred [13]. By doing this and replacing all time-ordering operators with contour-ordering operators $T_t \rightarrow T_C$, the theory for the non-equilibrium case can be reused with some changes. According to the Langreth theorem [13], the self-energies now get contour ordered counter parts $\Sigma^{>/<}$ and $\Sigma^{R/A}$. With $U(t)$ containing all time-dependence of H, the equations of motion becomes

$$\begin{aligned} \big(i\hbar\frac{\partial}{\partial t_1} &- E_k - U(t_1)\big) G^{R/A}(\mathbf{k}, t_1, t_2) \\ &= \hbar\delta(t_1 - t_2) + \int \frac{dt}{\hbar} \Sigma^{R/A}(\mathbf{k}, t_1, t) G^{R/A}(\mathbf{k}, t, t_2) \qquad (41) \\ \big(i\hbar\frac{\partial}{\partial t_1} &- E_k - U(t_1)\big) G^{<}(\mathbf{k}, t_1, t_2) \\ &= \int \frac{dt}{\hbar} \left[\Sigma^R(\mathbf{k}, t_1, t) G^<(\mathbf{k}, t, t_2) + \Sigma^<(\mathbf{k}, t_1, t) G^A(\mathbf{k}, t, t_2)\right]. \qquad (42) \end{aligned}$$

These are solved by the Keldysh relation [13]

$$G^<(\mathbf{k}, t_1, t_2) = \int \frac{dt}{\hbar} \int \frac{dt'}{\hbar} G^R(\mathbf{k}, t_1, t) \Sigma^<(\mathbf{k}, t, t') G^A(\mathbf{k}, t', t_2). \tag{43}$$

The Fourier transform gives the corresponding relations in frequency-space, taking into account the harmonic time-variation of all quantities.

6 Hamiltonian

The model takes into acount many different interactions and potentials, and for clarity and convenience it is split up in smaller parts containing similar terms. The full Hamiltonian reads

$$\begin{aligned} H &= T + V_{\mathrm{SF}} + V_{\mathrm{MF,\ static}} + V_{\mathrm{MF}}(t) + H_{\mathrm{AC}}(t) \\ &\quad + H_{\mathrm{LO\ phon}} + H_{\mathrm{Acc\ phon}} + H_{\mathrm{Int}} \\ &\quad + H_{\mathrm{Imp}} + H_{\mathrm{Alloy}} \\ &= \sum_{\alpha\beta,k} U_{\alpha\beta}(k,t) a^{\dagger}_{\alpha}(k) a_{\beta}(k) + H_{scatt} \end{aligned}$$

where quantities explicitly depending on time are denoted by a bracketed t. T is simply the kinetic part, V_{SF} is the heterostructure potential and static external bias, V_{MF} contains the mean field from the carriers and is divided into one time-dependent (with harmonic variation) and one static part. $H_{\mathrm{LO\ phon}}$, $H_{\mathrm{Acc\ phon}}$, H_{Int}, H_{Imp} and H_{Alloy} are the scattering terms for longitudinal optical and acoustic phonons, interfaces, impurities (doping), and alloy scattering (effective treatment of the non-crystalline AlGaAs) respectively, and are treated with self-energies within the self-consistent Born approximation (40). Finally, $H_{\mathrm{AC}}(t)$ contains the interaction with the (classical) electro-magnetic field, giving rise to absorption/gain effects. In the following sub-sections these parts will be described separately.

6.1 Single-particle Hamiltonian

The single particle Hamiltonian H_0 contains all one-particle energies and potentials, no scattering or interaction with electro-magnetic fields. It contains the kinetic energy operator, the static electric field and the mean field from the electron density and the doping. It can be decomposed as

$$H_0 = T + V^{SF} + V^{MF} = \sum_{\alpha\beta,\vec{k}} (T_{\alpha\beta} + U^{SF}_{\alpha\beta} + U^{MF}_{\alpha\beta}) a^{\dagger}_{\beta}(\vec{k}) a_{\alpha}(\vec{k}). \tag{44}$$

The kinetic part is

$$T_{\alpha\beta} = \delta\alpha\beta \left(\frac{\hbar^2 k^2}{2m(z)} + E^{\nu} a^{\nu\dagger}_{n} a^{\nu}_{n} \right) + \sum_{h=1}^{\infty} T^{\nu}_{h} \left(a^{\nu\dagger}_{n} a^{\nu}_{n+h} + a^{\nu\dagger}_{n} a^{\nu}_{n-h} \right) \tag{45}$$

and the static potential

$$U^{SF}_{\alpha\beta}(z) = V_{\mathrm{CB}}(z)\delta_{\alpha\beta} - eFz_{\alpha\beta}, \tag{46}$$

where $V_{\mathrm{CB}}(z)$ is the heterostrucure potential. The mean field potential $\phi^{MF}(z)$ is calculated from the electron density

$$\rho_{\mathrm{el}}(z,t) = \sum_{\alpha\beta} \sum_{k} \frac{2(\mathrm{spin})e}{A} \rho_{\alpha\beta}(k,t) \varphi^{*}_{\beta}(z) \varphi_{\alpha}(z), \tag{47}$$

where A is the in-plane area and $\rho_{\alpha\beta}$ is given by equation (32). $\phi^{MF}(z)$ is obtained by solving Poisson's equation

$$\nabla^2\phi^{MF}(z) = -\frac{\rho_{\mathrm{el}}(z) + \rho_{\mathrm{dope}}(z)}{\epsilon_0} \tag{48}$$

using the boundary condition $\phi^{MF}(z+d) = \phi^{MF}(z)$, with the solutions

$$\phi^{MF}(z,t) = \sum_h e^{ih\Omega t}\phi_h^{MF}(z). \tag{49}$$

$\phi_h^{MF}(z) = \frac{1}{T}\int dt\phi^{MF}(z)e^{ih\Omega t}$ is taking into account the harmonic time variations of the alternating light field and can be split into a time-dependent and a time-independent part. The mean field potential is thus given by

$$U_{\alpha\beta,h}^{MF}(z) = e\varphi_\alpha^*(z)\phi_h^{MF}(z)\varphi_\beta(z). \tag{50}$$

6.2 Electro-magnetic Field

The Hamilton operator from classical mechanics for a charged particle in an electro-magnetic field reads

$$H_{\mathrm{EM}} = \frac{(\mathbf{p} - e\mathbf{A})^2}{2m} + e\phi. \tag{51}$$

Thus the Hamiltonian for the electro-magnetic field in second quantization is

$$\begin{aligned} H_{\mathrm{EM}} &= \int d^3r\Psi^\dagger(\mathbf{r})\Big(-\hbar^2\nabla\frac{1}{2m(z)}\nabla + i\hbar\frac{e\mathbf{A}(z,t)}{2m(z)}\nabla \\ &+ i\hbar\nabla\frac{e\mathbf{A}(z,t)}{2m(z)} + \frac{e^2\mathbf{A}(z,t)}{2m(z)} + e\phi(z,t)\Big)\Psi(\mathbf{r}) \\ &= \int dz\sum_{\alpha\beta}\sum_{\mathbf{k}} a_\beta^\dagger(\mathbf{k})\left(T_{\alpha\beta} + U_{\alpha\beta}^{\mathrm{AC}}\right)a_\alpha(\mathbf{k}). \end{aligned} \tag{52}$$

The kinetic term $T_{\alpha\beta}$ we have already put into H_0, and so we subtract it from the electro-magnetic field Hamiltonian,

$$H_{\mathrm{AC}} = H_{\mathrm{EM}} - T = \sum_{\alpha\beta,\vec{k}} a_\beta^\dagger(\vec{k})U_{\alpha\beta}^{\mathrm{AC}}a_\alpha(\vec{k}). \tag{53}$$

In Coulomb gauge, with $\nabla\cdot\vec{A} = 0$ this gives

$$U_{\alpha\beta}^{\mathrm{AC}} = \int dz\frac{i\hbar A(z,t)}{2m(z)}\left(\varphi_\beta^*(z)\frac{\partial\varphi_\alpha(z)}{\partial z} - \frac{\partial\varphi_\beta^*(z)}{\partial z}\varphi_\alpha(z)\right) + \frac{e^2A(z,t)^2}{2m(z)}\varphi_\beta^*(z)\varphi_\alpha(z). \tag{54}$$

6.3 Phonon Scattering

The phonon terms $H_{\text{LO phon}}$ and $H_{\text{Acc phon}}$ are treated similarly with the self energy

$$\begin{aligned}\Sigma^{<}_{\alpha\alpha'}(E) &= \sum_{\beta\beta'} X^{-}_{\alpha\alpha'\beta\beta'} f(E_p) \int_0^{\infty} dE_k G^{<}_{\beta\beta'}(k, E - E_p) \\ &+ \sum_{\beta\beta'} X^{+}_{\alpha\alpha'\beta\beta'} [f(E_p) + 1] \int_0^{\infty} dE_k G^{<}_{\beta\beta'}(k, E + E_p) \qquad (55)\end{aligned}$$

and

$$\begin{aligned}\Sigma^{R}_{\alpha\alpha'}(E) = \sum_{\beta\beta'} X^{-}_{\alpha\alpha'\beta\beta'} [f(E_p) + 1] \int_0^{\infty} dE_k G^{R}_{\beta\beta'}(k, E - E_p) + \\ \sum_{\beta\beta'} X^{+}_{\alpha\alpha'\beta\beta'} [f(E_p)] \int_0^{\infty} dE_k G^{R}_{\beta\beta'}(k, E + E_p) + \\ \frac{1}{2} \sum_{\beta\beta'} X^{-}_{\alpha\alpha'\beta\beta'} \int_0^{\infty} dE_k G^{<}_{\beta\beta'}(k, E - E_p) \\ -\frac{1}{2} \sum_{\beta\beta'} X^{+}_{\alpha\alpha'\beta\beta'} \int_0^{\infty} dE_k G^{<}_{\beta\beta'}(k, E + E_p) \\ +i \int \frac{dE''}{2\pi} P\left\{\frac{1}{E''}\right\} \Big[\sum_{\beta\beta'} X^{-}_{\alpha\alpha'\beta\beta'} \int_0^{\infty} dE_k G^{<}_{\beta\beta'}(k, E - E_p - E'') \\ - \sum_{\beta\beta'} X^{+}_{\alpha\alpha'\beta\beta'} \int_0^{\infty} dE_k G^{<}_{\beta\beta'}(k, E + E_p - E'') \Big]. \qquad (56)\end{aligned}$$

The X matrices are just the collected terms for the coupling between the electron and the phonon fields, which is approximated not to depend on k. E_p is the phonon energy, either $E_{\text{acc.}} = \hbar\omega_{\text{acc.}}$ or $E_{\text{opt.}} = \hbar\omega_{\text{opt.}}$. In the program we neglect the last two lines of equation (56).

The LO phonons play a crusial role as extraction and injection mechanisms in the QCL:s studied in this work. The LO phonon mode is the lattice vibration mode where the atoms oscillate towards one another. The interaction with the resulting electric potential and an electron is called the *Frölich interaction*, and is particularly strong in III-V semiconductors since the basis atoms are partly ionised[17].

6.4 Elastic Scattering

The terms H_{Int}, H_{Imp} and H_{Alloy} constitute the elastic scattering and are treated with a common self-energy

$$\Sigma^{</R}_{\alpha\alpha'}(E) = \sum_{\beta\beta'} X^{elast}_{\alpha\alpha'\beta\beta'} \int_0^{\infty} dE_k G^{</R}_{\beta\beta'}(k, E), \qquad (57)$$

where the X^{elast} matrices again collects all the terms for the transition coupling for interface, impurity and alloy scattering.

7 Current

The quantum mechanical current is defined as

$$\begin{aligned} J(z,t) &= \frac{e}{V}\frac{\partial \hat{z}}{\partial t} = \frac{e}{V}[\hat{z}, H] = \\ &= e\sum_{\alpha\beta}\Big[\frac{\hbar}{i2m(z)}\left(\varphi^*_\beta(z)\frac{\partial\varphi_\alpha(z)}{\partial t} - \frac{\partial\varphi^*_\beta}{\partial t}\varphi_\alpha(z)\right) - \\ &- eA(z,t)\frac{\varphi^*_\beta\varphi_\alpha(z)}{m(z)}\Big]\frac{2}{A}\sum_{\mathbf{k}}\rho_{\alpha\beta}(\mathbf{k},t) \end{aligned} \tag{58}$$

where V is the volume of the sample and A is the cross-sectional area of the sample. This is in principle independent of z, but since it is impossible to account for all states in a numerical calculation it has proved to be more stable to take the mean value of the current over one period [18]. Doing this and collecting the terms in phase ($J^{\cos}$) and out of phase ($J^{\sin}$), as well as the direct current part (J_{dc}),

$$\langle J(t)\rangle = J_{\mathrm{dc}} + j_{\mathrm{ac}}(t) = J_{\mathrm{dc}} + J_1^{\cos}\cos(\Omega t) + J_1^{sin}\sin(\Omega t). \tag{59}$$

Here we used $\rho_{\alpha\beta} = \sum_h \rho_{\alpha\beta\rho}e^{ih\Omega}$ with $h \leq 2$ and $A = F_{\mathrm{ac}}\cdot(-ie^{-i\Omega t} + ie^{i\Omega t})/2\Omega$. We recall that in linear response, the alternating current can be written in complex form as

$$\begin{aligned} J_{\mathrm{ac}}(t) &= \Re\{\tilde{J}e^{-i\Omega t}\} = \Re\{\tilde{\sigma}F_{\mathrm{ac}}e^{-i\Omega t}\} = \Re\{(\sigma' + i\sigma'')F_{\mathrm{ac}}(\cos\Omega t - i\sin\Omega t)\} \\ &= \Re\{\sigma\}F_{\mathrm{ac}}\cos(\Omega t) + \Im\{\sigma\}F_{\mathrm{ac}}\sin(\Omega t), \end{aligned} \tag{60}$$

so we can identify $\Re\{\sigma\} = J_1^{\cos}/F_{\mathrm{ac}}$ and $\Im\{\sigma\} = J_1^{\sin}/F_{\mathrm{ac}}$.

8 Gain

In a material where Ohm's law $\vec{J} = \sigma\vec{E}$ is valid, the curl of the magnetic field becomes [19]

$$\nabla\times H = -i\omega(\epsilon_r\epsilon_0 + i\sigma/\omega)\vec{E}, \tag{61}$$

where ϵ_r is the static dielectric constant. On the other hand we may interpret the a.c. currents as shifts in the polarization:

$$\nabla\times H = -i\omega\epsilon(\omega)\vec{E}. \tag{62}$$

Thus we identify $\epsilon(\omega) = \epsilon_r\epsilon_0 + i\sigma/\omega$, or

$$\sigma = -i\omega(\epsilon(\omega) - \epsilon_r\epsilon_0) \tag{63}$$

The complex wave vector of the a.c. field is written $k = \beta + i\alpha/2$, where α is the absorption coefficient giving rise to a decay of the intensity $I \propto e^{-\alpha z}$ as the wave propagates through the material. The phase velocity relates the wavevector to the dielectric function by

$$v_{\text{phase}} = \frac{\omega}{k} = \frac{1}{\sqrt{\mu\epsilon(\omega)}}, \tag{64}$$

giving the system of equations

$$\begin{cases} \beta^2 - \frac{\alpha^2}{4} & = \frac{\omega^2}{c^2}\Re\left\{\frac{\epsilon}{\epsilon_0}\right\} \\ \beta \cdot \alpha & = \frac{\omega^2}{c^2}\Im\left\{\frac{\epsilon}{\epsilon_0}\right\}. \end{cases} \tag{65}$$

Solving (65) for α and taking ω large,

$$\alpha \approx \frac{\Re\{\sigma\}}{c\epsilon_0\sqrt{\epsilon_r}} = \frac{J_1^{\cos}}{F_{ac}c\epsilon_0\sqrt{\epsilon_r}}. \tag{66}$$

We see that the gain of the sample (the negative of the absorption α) can be obtained by calculating the amplitude of the part of the current that is in phase with the applied electric field, $j^{\cos}$.

Part II

Results

9 Scalari Quantum Cascade Laser[2] [1]

We start the discussion of the results with the simplest possible structure, as mentioned in the introduction to this thesis. It has only two wells per period and it is basically a three-level system, the minimum number of levels possible for a cascade lasing scheme[11]. The sample was produced by a research group at the Institute of Quantum Electronics in Switzerland[2] in 2010. The first author is G. Scalari, and we will simply call this structure the Scalari QCL. The group reported a measured gain with laser frequencies from 2.8 to 4.1 THz, up to a temperature of 125 K, although their simulations using a density matrix model indicated it could operate at temperatures above 200 K. Owing to the simple conduction band profile, the device is bi-polar and can be operated with both positive and negative bias voltages. However, we show here only results of a positive bias voltage.

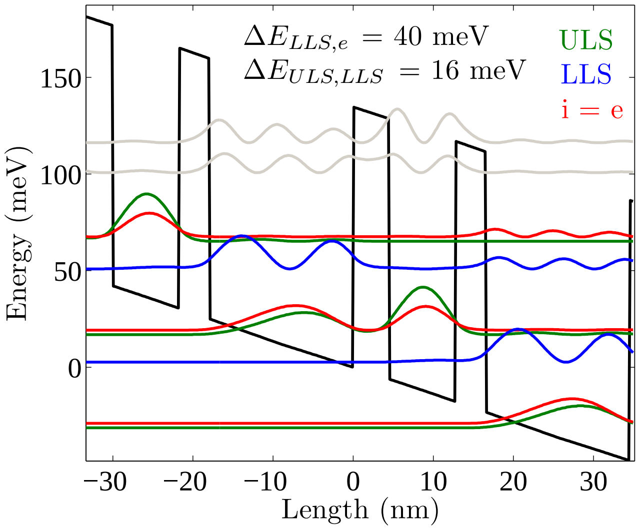

Figure 7: Conduction band structure and Wannier-Stark states at a bias per period of 48.25 mV, for the Scalari QCL.

This sample is well suited for studying in order to getting to know the program, since it has a very simple structure. It is also examined in some detail to find out

---

[1] This structure was simulated in cooperation with David Winge, Division of Mathematical Physics, Lund University.

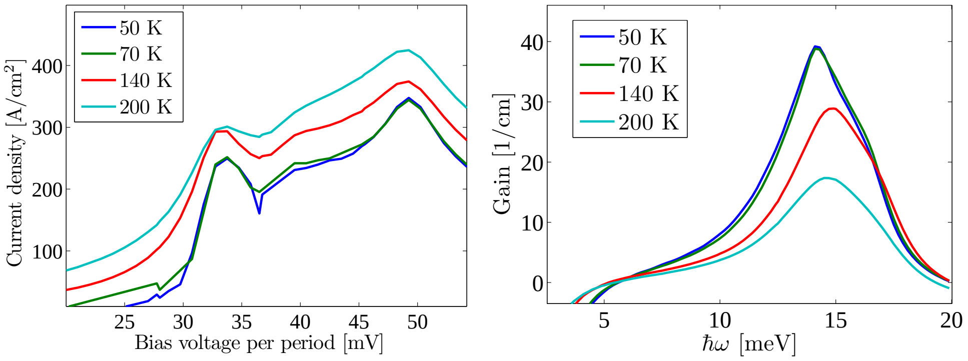

(a) (b)

Figure 8: (a) IV characteristics and (b) gain for the QCL by [2] for different temperatures of the Scalari QCL.

why the group's gain simulations did not compare very well with the experiment at higher temperatures.

The conduction band structure is shown in figure 7. The Wannier-Stark states are calculated at a bias of 48.25 mV per period since this corresponds roughly to the reported bias applied over the structure during operation (14 kV/cm = 48.3 mV/period). We see that the lasing would come from the transition from the blue state (the upper laser state ULS) to the green state (the lower laser state LLS), when a photon with energy $\hbar\omega = E_{ULS} - E_{LLS} \approx 15$ meV de-excites an electron by stimulated emission. The carriers in the LLS then rapidly transfer by emitting a longitudinal optical (LO) phonon of energy $E_{\mathrm{LO}} = 36.7$ meV, into the red state. Through resonant tunnelling via the red and the green state, the carriers are injected into the ULS of the next period downstream in potential.

Our simulated current is shown in figure 8(a). The current shows a peak at around 49 mV/period, which corresponds to the reported operating bias. This is where the gain is expected to be largest, since a high current indicates efficient scattering and tunnelling channels are quickly emptying the LLS. The current is too small here compared to the experiment, where the current densities are over 800 A/cm^2.

Figure 8(b) shows our resulting gain spectra. The gain is peaked around $\hbar\omega =$ 14-15 meV, corresponding to a frequency 3.4-3.6 THz. Assuming waveguide losses of about 20 cm^{-1}[20] (or possibly higher), the spectra indicates that lasing would stop somewhere between 140 and 200 K, i. e. at too high a temperature compared to the measurements.

There is a second current peak in figure 8(a) at a smaller bias of around 33 mV per period, than the main peak. At this bias, the ULS aligns with the LLS. This peak is not seen in the experiment, even though the alignment of the levels is real.

The reason why it is not visible ought therefore to be that something is suppressing the tunnelling current through the aligning states in reality, but is missing in our model. Our model does not take into account electron-electron scattering which, at low temperatures, helps in thermalising the carriers. Without this scattering, the electrons can get stuck in states with E_k far above the sub-band edge since they cannot exchange energy with the surroundings. To effectively compensate for this, it is possible to make other scattering mechanisms stronger, e. g. the acoustic phonon scattering by artificially increasing the deformation potential of AlGaAs, which increases the acoustic phonon-electron coupling strength. The acoustic phonons are not fully taken into account, however, but are simulated by a single, fully populated, acoustic phonon mode with energy $\sim k_B T$.

The pre-peak in the current simulation is indeed suppressed by increasing the deformation potential, as can be seen in figure 9(a). For higher temperatures, 10 times is too much of an increase, and the peak is still present for an increase of 5 times. The way we have thermalised the carriers is of course a very crude one and it doesn't have much of a quantitative value. However, it can still show the importance of electron-electron scattering for some quantum cascade structures. For negative biases, an even larger pre-peak was seen, and although suppressed, it is still present at even 10 times the normal deformation potential. With the deformation potential increased, we also approached the currents observed by [2].

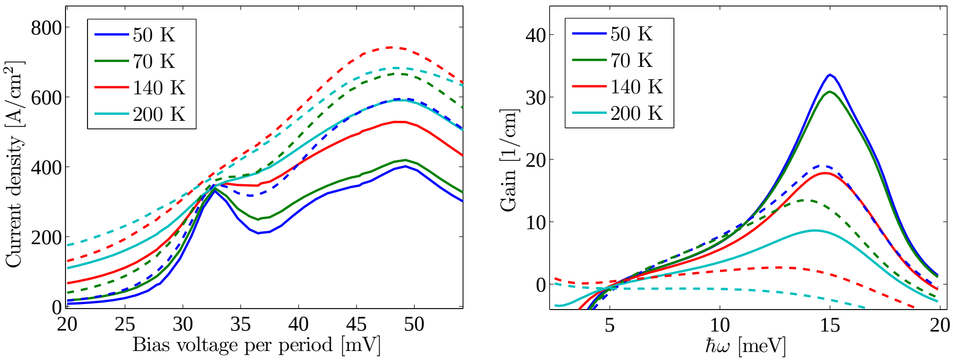

(a) (b)

Figure 9: (a) IV characteristics and (b) gain for the Scalari QCL for different temperatures and deformation potentials. Solid lines: 5 times the normal deformation potential. Dashed lines: 10 times the normal deformation potential.

In order to study the effect on carrier thermalisation when increasing the deformation potential, the carrier densities for different values of the deformation potential are plotted in figures 10(a)-(f). The bias is chosen at the operation point since here we can directly see how thermalisation is affecting the performance of the laser. The conduction band edge and the Wannier-Stark states are shown in white. The colour signifies the space and energy resolved electron densities. At T = 50 K, there are many carriers occupying higher k-states belonging to the LLS; thus, the carriers are not thermalised. At T = 140 K, the carriers are not so much accumulated at high k-values, thus the carriers are more thermalised. Increasing the deformation potential, we see that carriers are able to come down to states lying closer to the mini-band edge, by scattering via acoustic phonons. For low temperatures it is reasonable we have to increase the deformation potential more than for higher temperatures, since then more scattering is taking place even without this increase. For instance, the carriers in figure 10(e) are about as much thermalised as the ones in figure 10(d).

To investigate why the pre-peak at a bias per period of about 33 mV is reduced in figure 9(a), the current densities are plotted at this bias for two values of the deformation potential in figure 11(a). In this figure, the colour represents the space and energy resolved current density. Again we see that the carriers are not thermalised at T = 50 K, and current is carried through k-states of energy high above the sub-band edges. In contrast, when we increase the deformation potential 10 times as shown in figure 11(b), the electrons get much more thermalised, and the current flow is closer to the bottom of the sub-bands. Thus, the lack of electron-electron scattering could explain why we see the pre-peak in the current simulation.

The increase of the deformation potential heavily affects the gain of the device; the larger the thermalisation of the carriers, the lower the gain. In order to explain this, consider the densities in figures 10(a) and 10(e). In the first case, electrons occupy states of high E_k, thus there are more laser transitions possible than for the latter case, where most of the electrons sit near the mini-band edge. Thus the gain would be expected to get more spread out and overall lower, and this effect can be seen in figures 8(a) and 9(a). The group did not measure the gain directly as this is difficult to do, but the gain curves in figure 8(b) suggest lasing terminates at a temperature between 70 K and 140 K, in accordance with the experiment.

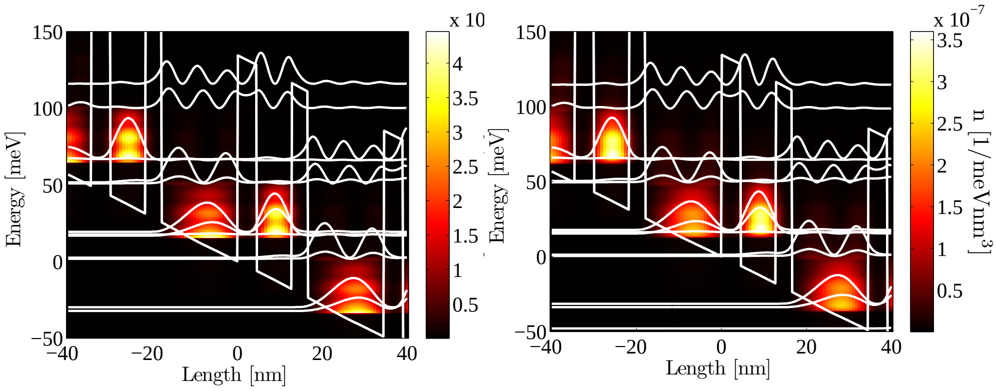

(a) T = 50 K

(b) T = 140 K

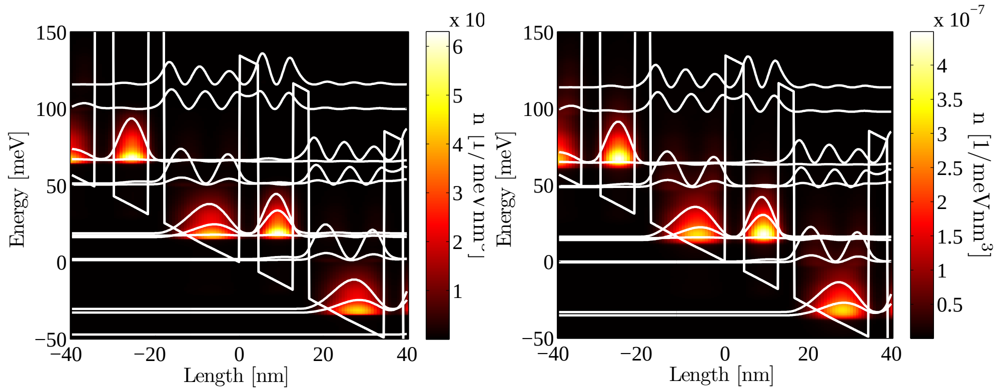

(c) T = 50 K

(d) T = 140 K

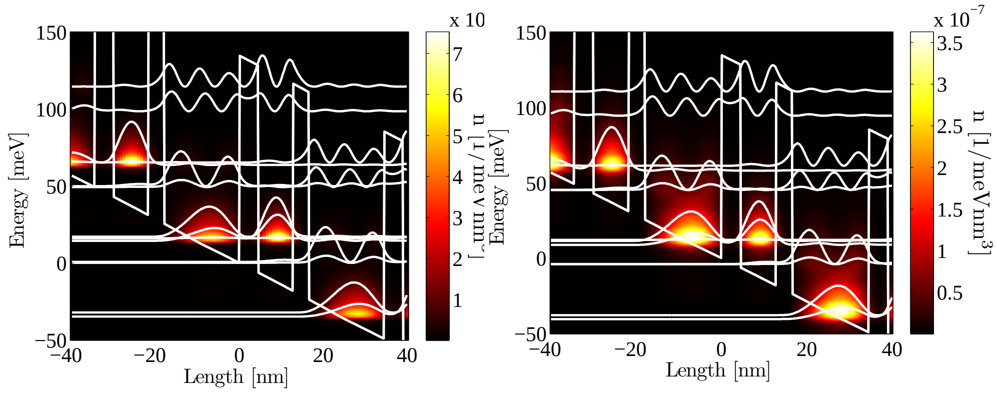

(e) T = 50 K

(f) T = 140 K

Figure 10: Carrier densities for the Scalari QCL for deformation potentials of 1 (top), 5 (middle) and 10 (bottom) times the normal. The bias is 49.25 mV/period.

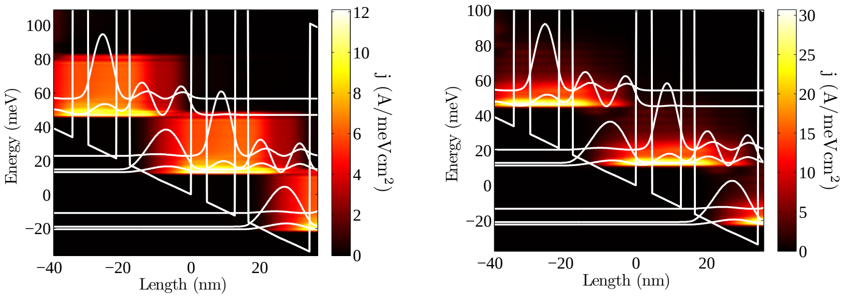

(a)

(b)

Figure 11: Current densities and Wannier-Stark states for the Scalari QCL at a bias voltage of 33.75 mV per period, for normal deformation potential (a) and 10 times the normal deformation potential (b).

10 V843 Quantum Cascade Laser[1]

This device is a THz QCL made from GaAs wells and $Al_{0.25}Ga_{0.75}As$ barriers. The structure was developed by a group at the Institute for Microscopical Sciences, NRC, Ottawa, Canada. They call the sample V843, which we will also adopt in this text. The heterostructure was found through a genetic algorithm intended to maximise gain at T = 150 K. The laser is designed to operate at a bias voltage of 21 kV/cm = 76 mV/period. The structure is, starting with the injection barrier,

44/62.5/**10.9**/66.5/**22.8**/84.8/**9.1**/61 Å.

Lasing occurs at $\hbar\omega = 14.3$ meV in the measurements at an applied bias voltage of 76 meV/period. The structure is shown schematically in figure 12. The results of measurements and some of the simulation results shown in this section have been published together with the experimental group in the Journal of Applied Physics[1]. In the published text, the structure is called a “phonon-photon-phonon” design since it uses LO phonon emission for injection and extraction. The extraction energy ΔE_{ex} and injection energy ΔE_{in} match quite closely the LO phonon energy E_{LO}, as seen in figure 12. The carriers are entering the period via resonant tunnelling through the injection barrier, in the so-called injection level (i). They are then emitting a LO phonon and de-excites to the upper laser state (ULS). Here they are de-excited into the lower laser state (LLS) by emitting a photon. They are then again emitting a LO phonon to end up in the extraction level (e), where they tunnel into the next period and the whole thing is repeated again.

The aim would be to mach the injection and extraction energies with the LO phonon energy in order to get optimal injection and extraction rates. The genetic algorithm, however, optimised the structure for a number proportional to inversion n, oscillator strength Ω for extraction tunnelling and the inverse of

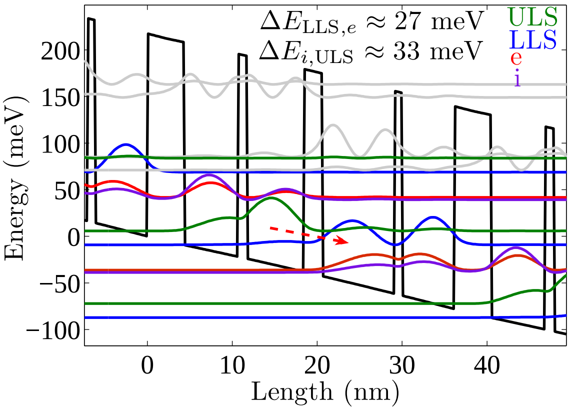

Figure 12: Conduction band profile of the V843 QCL, with an applied bias voltage of 78 mV/period. The arrow indicates the lasing transition with energy $\hbar\omega = 14.9$ meV. Given are the extraction and injection energies $\Delta E_{\mathrm{ex}} = E_{\mathrm{LLS}} - E_e$ and $\Delta E_{\mathrm{in}} = E_i - E_{\mathrm{ULS}}$, which are designed to match the optical phonon energy $E_{\mathrm{LO}} = 36.7$ meV. The states e and i are in resonance, allowing for tunnelling with a tunnelling coupling strength of $\hbar\Omega = 1.25$ meV, transferring carriers into the next period.

the period length $1/d$. The tunnelling coupling strength between the extraction levels for tunnelling across the extraction barrier is characterised by the oscillator strength $\hbar\Omega = \Delta E_{\mathrm{e1/e2}}$. The main scattering mechanism was assumed to be the LO phonons, but in spite this the difference between the injection and upper laser level energies are off the LO phonon energy by 9 meV, which was interpreted as an activation energy for phonon emission. The group wanted the injection barrier to be 44 Å thick in order to minimise the conduction by states higher in energy. The oscillator strength was not very large ($\hbar\Omega = 1.14$ meV).

10.1 Current and Gain simulations

The results of the current simulation are shown in figure 13. The peaks correspond very well with the measurements, in fact the agreement is quite remarkable. The peaks are of the same height, and the simulations nicely follow the experimental curve up the main peak. Even the two smaller bumps are reproduced by the NEGF simulations. These occur when several states align to construct a far-reaching tunnelling. The first peak is centred on 15.3 meV, when all states align in one band, running across two periods as shown in figure 14(a). The band repeats in energy and makes transport over two periods possible. At the second peak at 31.5 mV, the bands again align as in figure 14(b), but now the band runs over only one period. The bands are divided into sub-bands of even width in energy, which is an

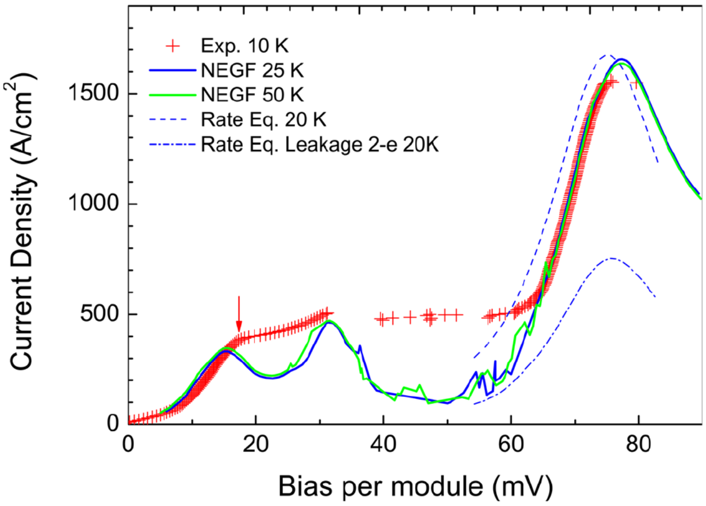

Figure 13: Simulated current density for different temperatures and comparison with rate equation model simulations and measurements by the experimental group. The dash-dotted line shows the contribution to the current from the wrong extraction channel from ULS (2) directly to the extraction level (e), simulated with the rate equation model.

artifact of discrete scattering mechanisms. The reason why the peaks are not so pronounced in the measurement is that a negative differential conductance (current decreasing with bias) gives rise to instabilities in the sample. The main peak is centered on 76-78 mV/period. The highest inversion between the lower and upper laser states was found at about 78 mV/period, where there is the most current, although it is only a marginal difference from the inversion at 76 mV/period. Here the energy levels are such that the optical phonon transitions and the extraction tunnelling rate are as most efficient.

Increasing the temperature would increase the effect of acoustic (and LO) phonon scattering, increasing broadening and thus the current. The temperature differences in figure 13 do not have a noticeable impact on the current, however.

The gain at different biases for T = 140 K is shown in figure 15(a). The gain is largest at a bias of 74 mV/period, which is in reasonable accordance with the experiment. We see a shift in energy, from around $\hbar\omega = 11.5$ to 14 meV (2.8 to 3.4 THz) as the bias goes from 72 to 78 mV/period. This shift was also observed in the measurements, and seen as a shift in lasing frequency (where the lasing can occur only at specific frequencies in resonance with the waveguide cavity) from 2.8 to 3.2 THz over a similar range of biases. This seems to agree well with our simulations.

It is also interesting to see how gain is affected by temperature, and for this

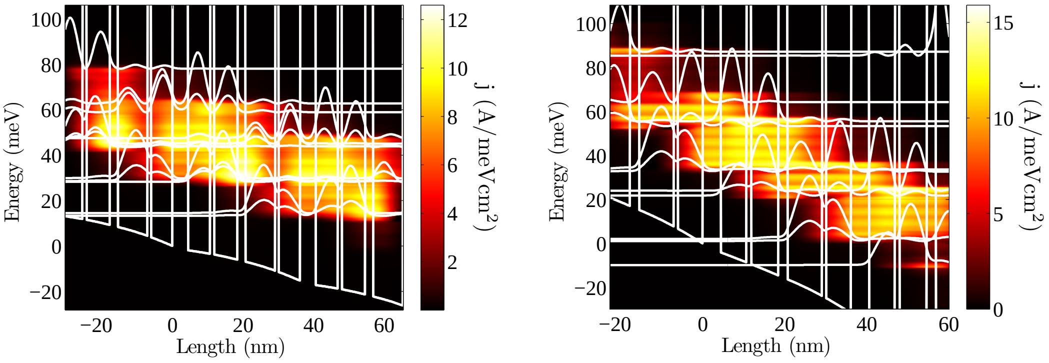

(a) (b)

Figure 14: Current densities at (a) 15.3 mV/period and (b) 31.5 mV/period at T = 50 K for the V843 QCL.

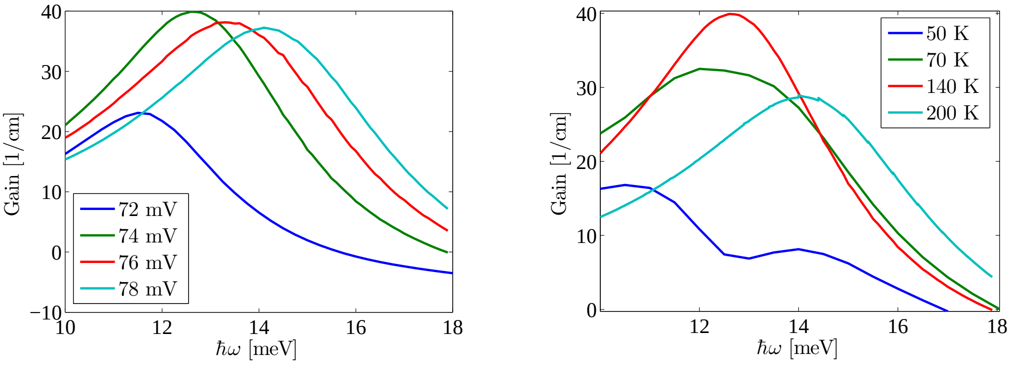

(a) (b)

Figure 15: Gain for the V843 QCL at (a) T = 140 K for different biases and (b) different temperatures at a bias of 74 mV/period, except for T = 200 K, where the bias per period is 78 mV.

reason the gain was simulated at T = 50, 70, 140 and 200 K which is shown in figure 15(b). We see that at very high temperatures (T = 200 K) the gain goes down. This is to expect since carriers are more likely to get thermally excited into the LLS from the extraction level, an effect called thermal backfilling. Other scattering effects also become more prominent at high temperature that would further reduce inversion. For low temperatures the gain goes down again, contrary to what is expected since scattering and backfilling is reduced. To explain this phenomenon, the carrier densities are plotted in figures 16(a) - 16(d). The energy difference between the LLS and the extraction level is not exactly matching that of the LO phonon, so it won't assist very efficiently in emptying it. We therefore get a build-up of charge carriers on the lower laser level side of the period, reducing inversion and also gain. For higher temperatures this effect is somewhat reduced due to increased scattering. For lower temperatures, the electrons get trapped at low energies in the lower laser level. We recall that the model does not take into account electron-electron scattering, which would counteract the trapping of electrons by increasing scattering. It is clear from figures 16(a) - 16(d) that inversion is highest at 140 K, which explains why the gain is highest for this temperature.

Assuming waveguide losses of about 20/cm[20] the model implies that lasing still takes place at 140 K and above. However, if we would include electron-electron scattering, the overall thermalisation would be increased and so we could expect the carrier density, and thereby gain, at 140 K to look more like the density and gain at 200 K. This is probably why our model gives a higher operating temperature than what is observed experimentally.

The gain curve at 50 K in figure 15(b) has two peaks, which suggests that there are two channels producing gain, the one higher in energy increasing with temperature until it overshadows the lower one. From the densities in figure 17(b) and the spectral function (33) $A(E, z)$ for $k = 0$ (which is basically the density of states), one would expect a peak at $\sim$ 12.6 meV, since this is the difference between the energy where the density of the upper laser state is maximal, and the energy where the density of states is largest in the lower laser state. In stead, it seems we get one peak at a lower and one at a higher energy.

The distance between the two peaks is too large to be explained solely by the energy difference between the extraction levels responsible for the resonant tunnelling. I was unable to find a good explanation to why these peaks occur, but the effect seems to still be present at 70 K, producing the broad gain peak seen in figure 15(b).

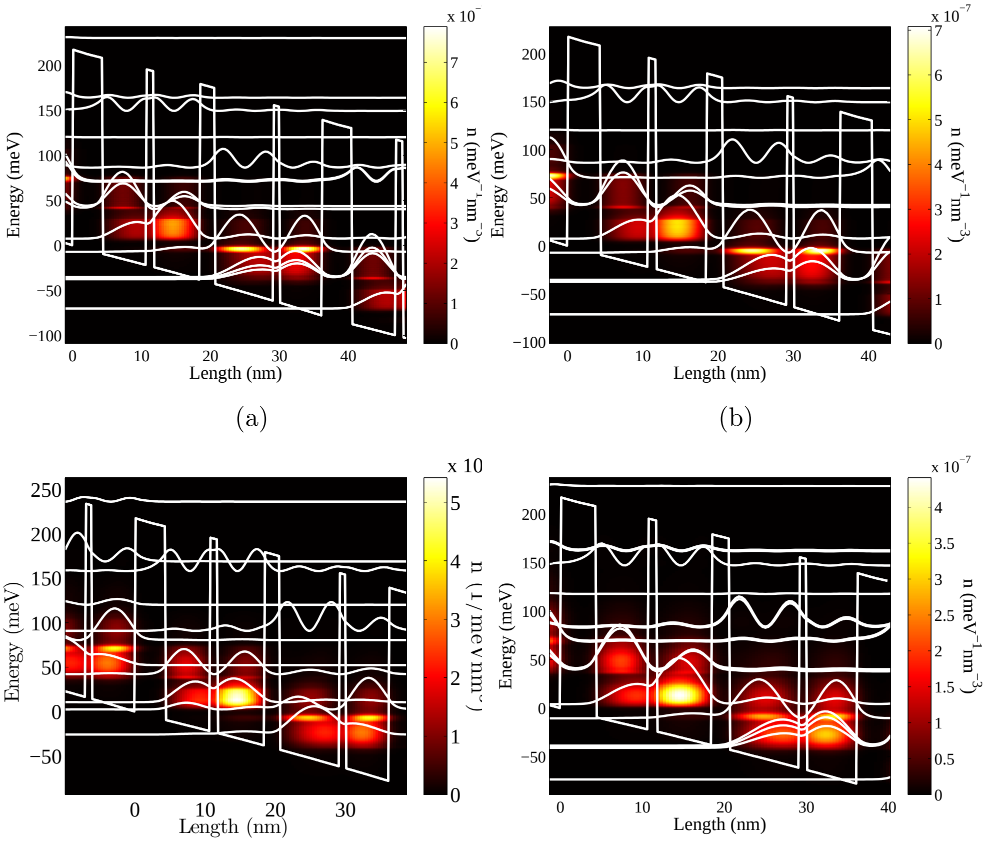

(a)

(b)

(c)

(d)

Figure 16: Carrier densities for the V843 QCL at (a) 50,(b) 70,(c) 140 and (d) 200 K for a bias of 78 meV/period

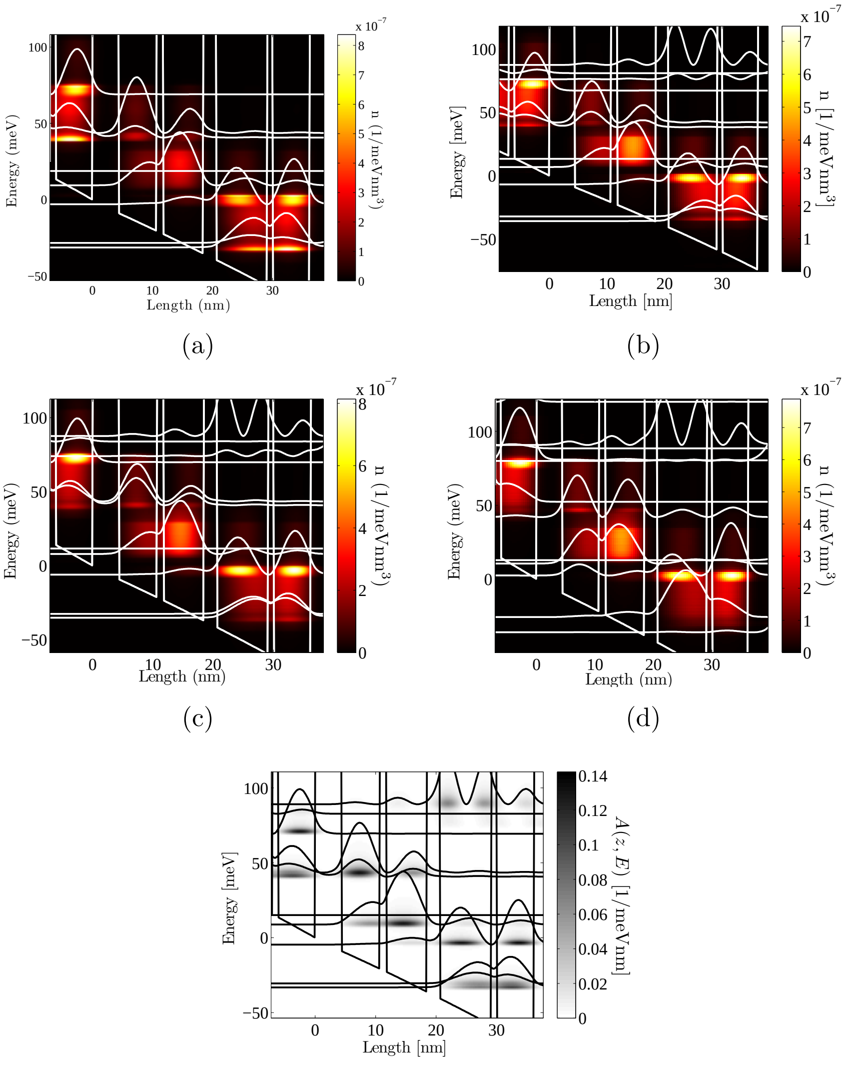

(a) (b) (c) (d) (e)

Figure 17: Electron densities for the V843 QCL at 50 K for (a) 72 mV, (b) 74 mV, (c) 76 mV and (d) 78 mV bias per period. (e) shows the spectral function $A(z, E)$ for $k = 0$ at 50 K and 74 mV/period.

10.2 Comparison with measurements

The current curves match closely the experiment. The first small peak is located at too small a bias in the simulations, and it appears that the current is more phonon driven in reality than the model predicts. The experiment showed the device lasing at 3.2 THz up to a temperature of 138 K, even though the NEGFT simulations showed gain of ~ 40 cm^{-1} at 140 K and thus implied gain at even higher temperatures than what the experiment found. Our assumption that the losses are about 20 cm^{-1} might be too optimistic, however. It is entirely possible that the losses are much greater than that, in which case the model would correspond closer to the measurements. When, at 140 K, the bias voltage was changed from 72 - 78 mV/period about the same shift from 2.8 at 72 mV/period to 3.5 at 78 mV/period, in lasing frequency as experimentally verified at 10 K was found. We argue that because of this similarity, due to the neglection of e-e scattering we simulate at 140 K the approximate thermalisation expected at 10 K experimentally.

10.3 Possible improvements of the structure

The carrier densities show that carriers get stuck in the LLS since the extraction by a LO phonon followed by tunnelling is not efficient enough, since $\Delta E_{\mathrm{LLS,e}} < E_{\mathrm{LO}}$ and the tunnelling coupling strength $\hbar\Omega$ is not very large. Thus, to improve gain, two features could be modified: the energy difference between the lower laser and the extraction levels could be increased to closer match the LO phonon, perhaps by making the second last well thinner, and the injection/extraction tunnelling barrier could be narrowed in order to increase $\hbar\Omega$. It may be hard to do both these things and still maintain good gain at the same frequency and bias, more so since the injection barrier needs some width in order to avoid couplings to high energy levels of the next periods. Decreasing the width of the barrier would increase the separation of the extraction levels, lower the peak gain in favour of two smaller gain peaks of separate frequency, so the thickness of the barrier can only be modified within some limits.

11 Quantum Cascade Laser by Ghasem Razavipour as of Jan 30th 2012

This design of a THz quantum cascade laser was sent to me from Ghasem Razavipour, a PhD student at the University of Waterloo, Canada on January 30th 2012 with a request to study the current and gain characteristics with NEGFT simulations. These simulations were to be compared to the student's simpler calculations with a density matrix model. The results significantly differed, the resulting gain being about half as much in NEGF simulations than what the density matrix model indicated. The structure was then altered in an attempt to improve the performance, and the attempt was indeed successful.

11.1 Structure

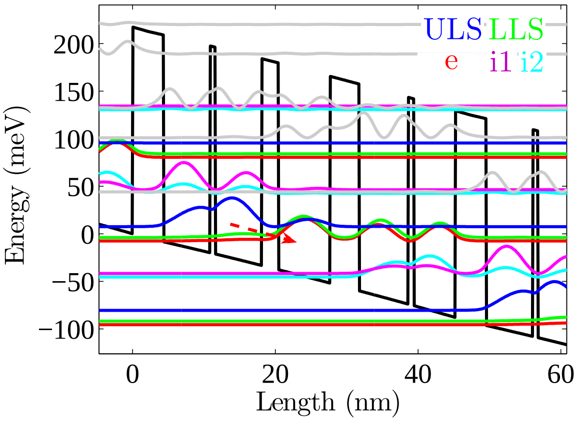

Figure 18: The structure with the squared Wannier-Stark states at 88 mV bias per period.

The material is GaAs/$\mathrm{Al}_{0.25}\mathrm{Ga}_{0.75}\mathrm{As}$ and the conduction band structure is

$$\underline{\mathbf{43}}/65.3/\mathbf{7.8}/65/\mathbf{23}/72.3/\mathbf{41}/68.5/\mathbf{8.55}/57.6$$

in Ångström, starting with a barrier. This makes one period 45.205 nm long. The band structure is shown in figure 18, together with the Wannier-Stark states. The operating bias should be 19.5 kV/cm $= 19.5 \cdot 10^3/10^7 \cdot 45.205 \approx 88$ mV/period.

This design uses the resonant-phonon extraction scheme where the electrons, after lasing from the ULS (blue) to the LLS (green), are first extracted by resonant tunnelling and then de-excited by an optical phonon. This design avoids problems with a second phonon channel going directly to the extraction state, had it been a simple phonon extraction as in the two samples studied previously. Now, this transition is too diagonal in space to be possible.

The extraction and injection energies correspond very well to $E_{\mathrm{LO}} = 36.7$ meV, $\Delta E_{\mathrm{in}} = 34.9$ and $\Delta E_{\mathrm{ex}} = 34.1$. The current channels should therefore be efficient enough to expect a high inversion. The resonant extraction states (LLS and e) are so close in energy that the contribution to the gain from each one largely overlap and thus one large gain peak is expected. The gain should be peaked around $E_{\mathrm{ULS}} - E_{\mathrm{LLS}} = 11.4$ meV.

11.2 Results

The simulated current is shown in figure 19(a). There is a small pre-peak, indicating our neglection of e-e scattering does not play a significant role for this structure. The main peak is at the designed operating bias and has a nice height,

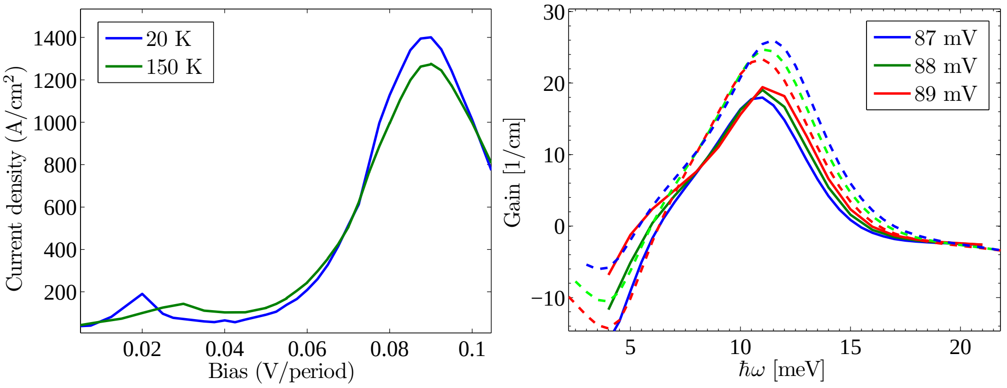

(a) (b)

Figure 19: Current (a) and gain (b) simulation results, where full lines are for $T = 150$ K and dashed are for $T = 20$ K.

so we have an efficient current path at this bias.

The gain is shown in figure 19(b). Despite the indications, the gain is surprisingly low. The gain is probably too low to have lasing at 150 K, and even at 20 K it is very low. It seems to be rather steady with temperature, however, and optimising this structure could possibly give a gain spectrum that is not strongly dependent on temperature.

This result differs significantly from the DM model, where a gain of 45 cm^{-1} was obtained for $T = 150$ K.

To see why the gain is so low we look at the carrier inversion, which at 20 K and 88 mV/period is $6 \cdot 10^9$ cm^{-2}, only 20 % of the doping, and at the same bias at 150 K it is $4.4 \cdot 10^9$ cm^{-2}. So, low inversion is what is causing the low gain, and the electron density at $T = 150$ K (shown in figure 20) can tell us why.

At a bias voltage of 88 mV/period, the density of the injection level is much smaller than that of the ULS, suggesting injection scattering is more efficient than extraction scattering. Furthermore, carriers are accumulated in the LLS before the extraction barrier, which implies that the extraction barrier is too thick for efficient tunnelling into the next period. If the extraction barrier is narrowed down from 41 Å, but the resonance between the extraction levels is still maintained, gain should increase. To test this hypothesis and see whether an improvement can be made, the extraction barrier was changed, as described in the following subsection.

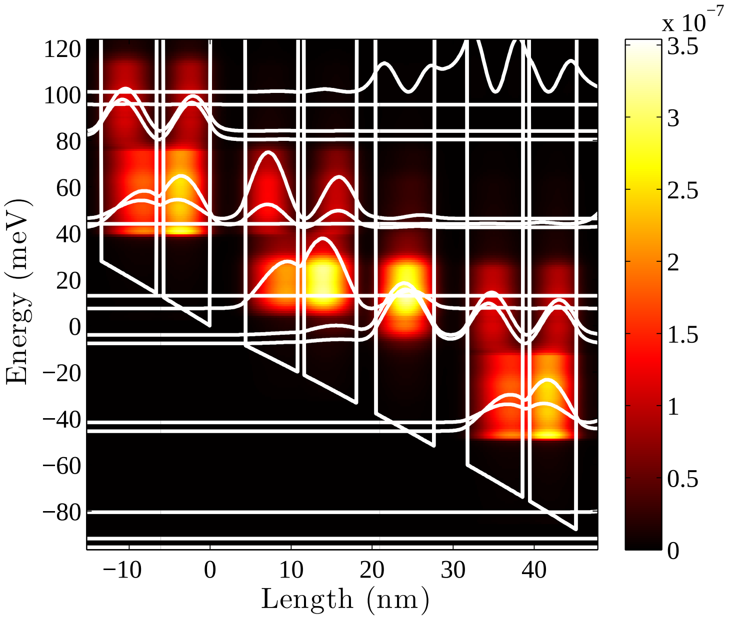

Figure 20: Carrier densities at 150 K for a bias of 88 mV per period.

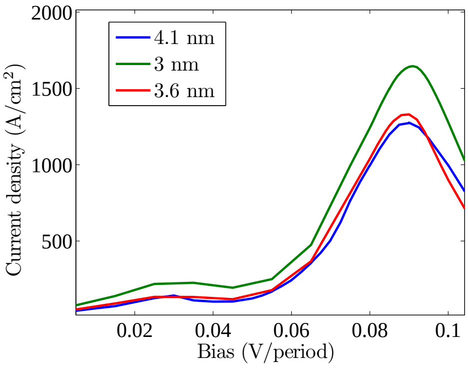

Figure 21: Current for the structure with three different extraction barrier thicknesses. 4.1 nm is the original thickness.

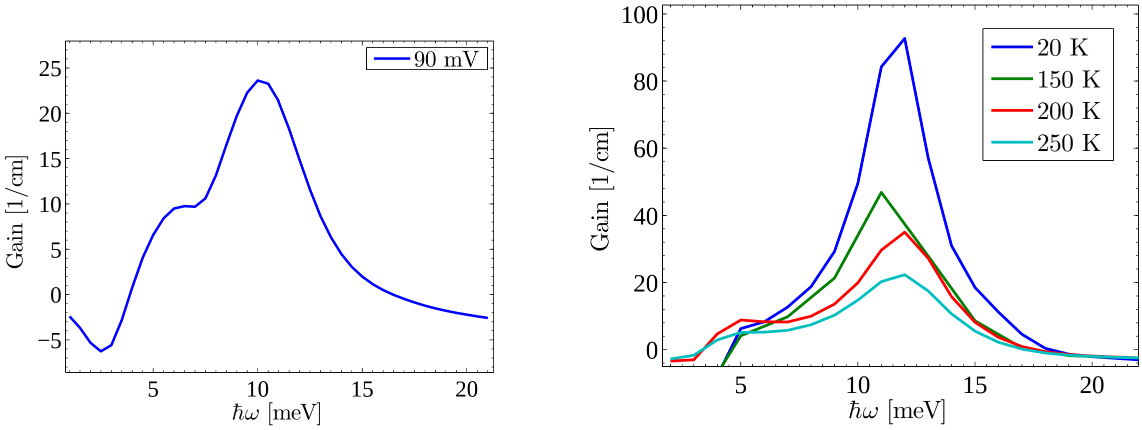

(a)

(b)

Figure 22: Gain for the altered structure with an extraction barrier of (a) 30 nm at $T = 150$ K and (b) 36 nm at the operation point for different temperatures.

11.3 Optimisation

The tunnelling rate depends on the tuning of the two extraction levels lying close in energy. When they are close enough, they form a binding (anti-symmetric) and anti-binding (symmetric) pair, and are said to be in resonance. This configuration gives a large transition matrix element for tunnelling, i. e. a large probability for electrons in the well to the left of the barrier to tunnel through to the right well. The same is true for electrons in the right well, which tunnel back into the left well. In this way the carriers are oscillating back and forth across the barrier, with a frequency of $\Omega = \Delta E_{\mathrm{L/R}}/\hbar$[21]. $\Delta E_{\mathrm{L/R}}$ is the energy difference between the resonant levels. Large Ω give a more efficient tunnelling rate from left to right since the electrons are quickly removed from the left side well. If the scattering is sufficiently high, the electrons will then emit a phonon and de-excite from the right side well before tunnelling back into the left one. $\hbar\Omega$ is called the tunnelling coupling strength across the barrier. In this (coherent) picture, narrowing the extraction barrier makes the states of the left and right wells overlap more and thus separate more in energy, giving a higher oscillation frequency Ω.

In order to optimise the structure, the extraction barrier was first narrowed down to 30 Å, to make the tunnelling through it more efficient. The effect on current is shown in figure 21, and we see that the narrow barrier increases the current by a fair amount. This means the scattering became more efficient, and since the only thing changed was the extraction barrier width, it must have been the extraction tunnelling rate that improved.

We see in figure 22(a) that gain increased slightly. There are now two distinct gain peaks, one for each of the extraction levels that are now separated by ≈ 5 meV . However, looking at the electron densities and the Wannier-Stark states in figures 23(a) and 23(c), the extraction levels are not in resonance any more since their energy difference is too large.

For this reason, the extraction barrier was set to 36 Å, a thickness also reported by the experimental group to have given the largest oscillator frequency so far in one of their QCL:s. Other groups have reported this is the best extraction barrier thickness as well[22].

For an extraction barrier of 36 Å the current (figure 21) is not increased so much, but the gain (figure 22(b)) is nearly twice the gain from the original structure. The gain spectrum show much less of the two gain peaks from each of the de-tuned extraction levels, which means the two levels overlap and their individual gain is added up. The densities and Wannier-Stark levels for this choice of extraction barrier is shown in figure 23(b). It is evident that the 36 Å barrier has much more inversion than the 30 Å one, where carriers accumulate in the extraction levels before the injection barrier. For this reason the tunneling rate does not seem to be as good for 30 Å barrier, and the oscillator strength $\hbar\Omega = 3.06$ meV is smaller than that for the 36 Å barrier $\hbar\Omega = 3.19$ meV. In figure 23(d) we see that once again the extraction levels are in resonance for the 36 Å barrier, which explains why the tunneling is more efficient than for the 30 Å barrier.

In figures 23(a) and 23(b) the densities for the structures with modified extraction barriers are shown. The fact that the current density is larger for the 30 Å barrier when the extraction states are not in resonance, than for the 36 Å barrier where they are, can be explained by carriers in the ULS also tunnel easier through the extraction barrier when it is narrowed down. The increased current then comes not only from the extraction tunneling, but from another channel that is opened up, but that does not contribute to the gain.

With the level of inversion of the 36 Å injection barrier structure, it seems the structure could not be optimised significantly more.

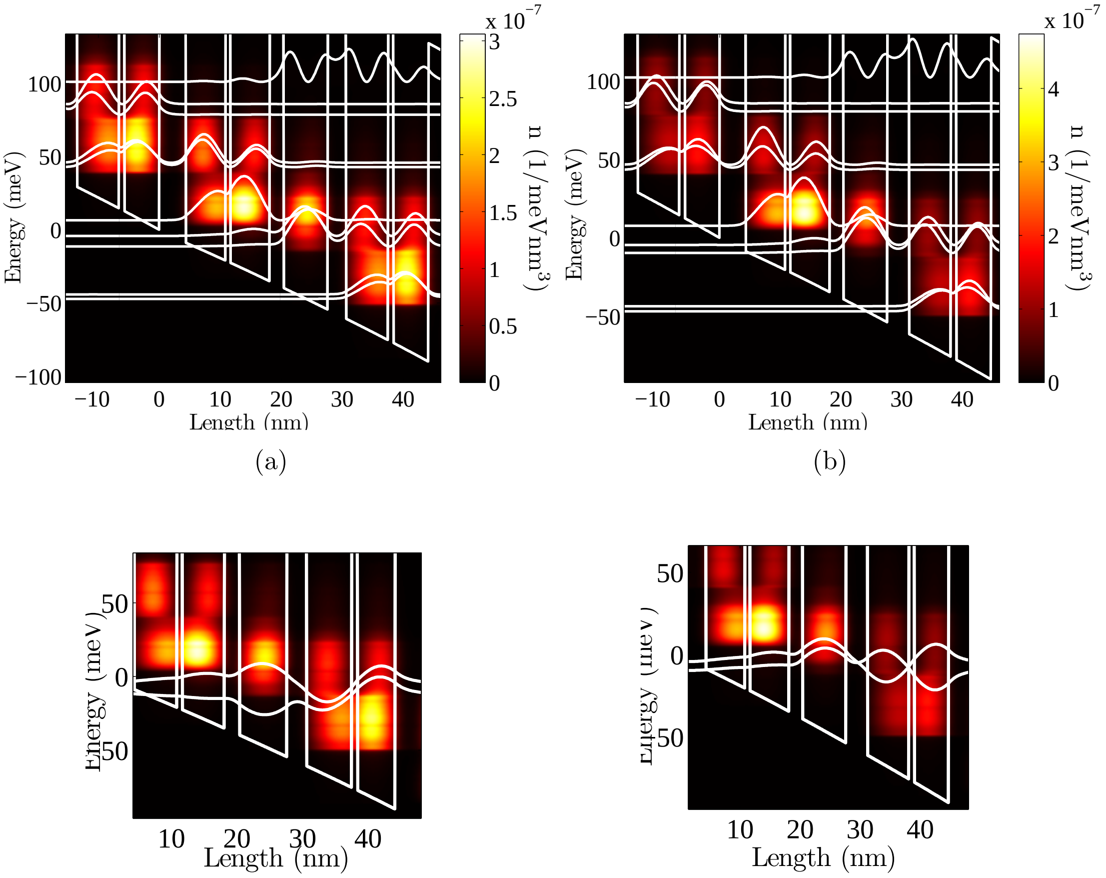

(a) (b)

(c) (d)

Figure 23: Carrier densities for the modified band structure with an extraction barrier of (a) 30 Å and (b) 36 Å, as well as the states (not squared) responsible for extraction tunneling through the extraction barrier for the structures with (c) 30 Å and (d) 36 Å extraction barrier.

12 Gendron Quantum Cascade Detector, Sample A[3]

We will now look at a quantum cascade photodetector (QCD), described in an article by L. Gendron et al.[3]. We will call this structure the Gendron QCD.

12.1 Structure

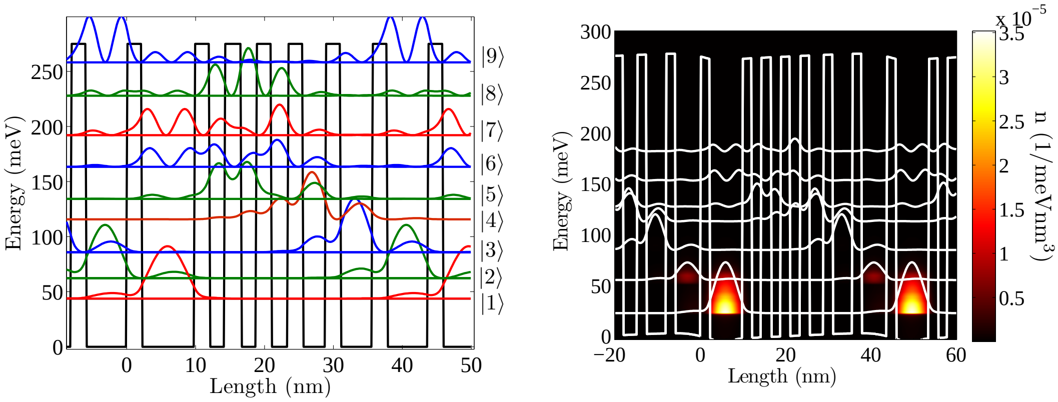

(a)

(b)

Figure 24: (a): The structure of the device with Wannier states. (b): Electron densities and the maxima of the spectral function $A(E, z)$ taken at $k = 0$ (white lines) at $T = 100$ K. The bands are plotted with the mean field potential.

This photodetector is shown in figure 24(a) and, in contrast to the Quantum Well Infrared Photodetector (QWIP), operates with no applied bias. It detects when an electron in the ground state $|1\rangle$ of the widest well absorbs a photon and is transmitted into one of the top most energy levels in the same well, $|6\rangle - |9\rangle$. The electron then tunnels across the barrier to the right into the next well and cascades down through one of several possible current paths via the states $|5\rangle$ to $|2\rangle$, to end up in level $|1\rangle$ of the next period. The cascaded electron thus induces a potential difference between the periods. When enough carriers are excited, this gives rise to a detectable current that is measured to detect the incoming light. In experiment, beside the current response to the light field, the absorption spectrum is also measured to control which excitation gives rise to the detection current.

The heterostructure consists of 7 GaAs wells of the widths

$$\underline{76}/23/23/23/34/45 \text{ Å}$$

and $Al_{0.34}Ga_{0.66}As$ barriers with widths of 22 Å.

12.2 Experimental Report

The experimental group reported a response spectrum at low temperature ($T =$ 50 K) with several absorption peaks, two being much stronger than the others. These peaks are attributed to the $|1\rangle$–$|5\rangle$ and $|1\rangle$–$|6\rangle$ transitions. The absorption measurement conducted at room temperature ($T = 300$ K) also showed the same characteristics. This is not desirable since if one detects a current, it is not clear from what peak the current stems, and thus it is impossible to know which frequency one detects.

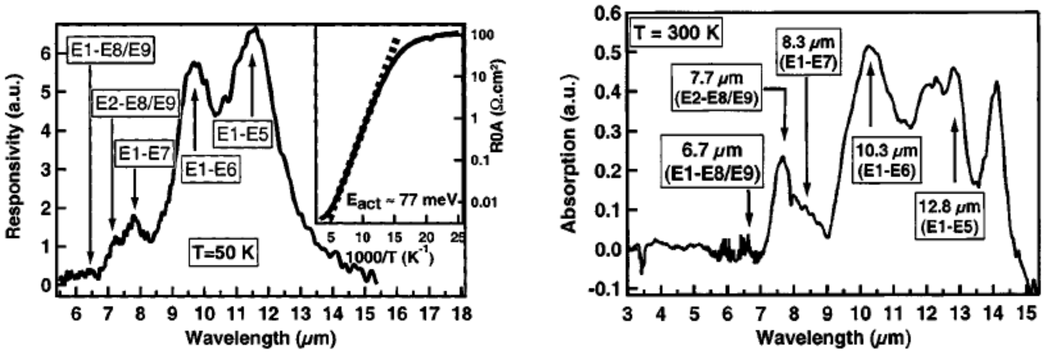

(a) (b)

Figure 25: (a): Experimentally measured response spectrum at $T = 50$ K. (b): Measured absorption spectrum at $T = 300$K. Both pictures are taken from Ref. [3]. For a description of the inset in (a), please refer to the source article.

The absorption measurements gave the following absorption peaks ($E = \frac{hc}{e\lambda}10^9[meV]$ where λ is measured in μm):

$$\begin{aligned}
|1\rangle \rightarrow |5\rangle: &\quad 97 \text{ meV} \\
|1\rangle \rightarrow |6\rangle: &\quad 120 \text{ meV} \\
|1\rangle \rightarrow |7\rangle: &\quad 149 \text{ meV} \\
|2\rangle \rightarrow |8\rangle/|9\rangle: &\quad 161 \text{ meV} \\
|1\rangle \rightarrow |8\rangle/|9\rangle: &\quad 185 \text{ meV.}
\end{aligned}$$

The peaks are quite broad, about 20 meV, which is a negative side of the QCD; it is not a very precise device.

12.3 Results

The Wannier states and the conduction band structure is shown in figure 24(a). In figure 24(b), a new concept to show the state of the system is proposed. Here, colour represents the carrier density. The white wavy lines are the maximum of the spectral function $A(E, z)$ (33) taken at $k = 0$, plotted along the growth direction where it has maxima in energy. The spectral function is basically the density of states, and so it is a good representation of where electrons are likely to be and what transitions are more probable than others. $A(E, z)$ also takes into account all scattering mechanisms and potentials in our model.

The spectral function in figure 24(b) shows 7 distinct energy levels, whereas there are 9 Wannier states altogether. This is because the density of states is very low for energies near the ionisation energy. The spectral function is plotted since the Wannier states do not give the correct energies (they do not take the self-energies or mean-field into account). The Wannier-Stark states are not plotted since for 0 bias, they are not defined. Instead, the mini-bands (corresponding to the electronic bands in atomic crystals) appear.

To explain and analyse the experimental findings, the group's measurements have been simulated with NEGFT, the results of the simulations are shown in figure 26.

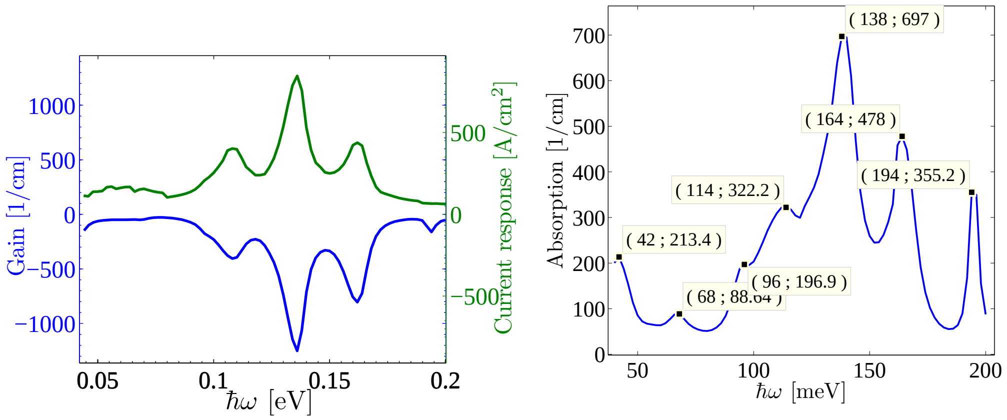

(a) (b)

Figure 26: (a): Current response and gain spectrum for the QCD by [3] at $T = 50$K, as well as (b): absorption spectrum at $T = 300$ K.

The peaks in the current response in figure 26(a) correspond well to the absorption peaks in the same figure, although some details seen in the experiment cannot be seen here. The main peaks are centred on $\hbar\omega = 110$, 136 and 162 meV. In the current spectrum there is also a small peak at 194 meV. These peaks are confirmed by the simulated absorption at $T = 300$ K, seen in figure 26(b). Here we can also see the features of the measurements missing in figure 26(a).

To explain the peaks, we look at the largest energy differences between the

Wannier states in figure 24(a). These are

$$\begin{aligned}\Delta E_{19} &\approx 214 \text{ meV}\\ \Delta E_{29} &\approx 196 \text{ meV}\\ \Delta E_{18} &\approx 184 \text{ meV}.\end{aligned}$$

The spectral function gives the energy differences

$$\begin{aligned}\Delta E_{17} &\approx 159 \text{ meV}\\ \Delta E_{16} &\approx 130 \text{ meV}\\ \Delta E_{15} &\approx 105 \text{ meV}.\end{aligned}$$

Looking at the Wannier states alone, the largest peaks should correspond to the transitions $|1\rangle \rightarrow |6\rangle$, $|1\rangle \rightarrow |7\rangle$ and $|2\rangle \rightarrow |9\rangle$. We therefore attribute the peaks in the spectra 26(a) and 26(b) to the transitions

$$\begin{aligned}|2\rangle \rightarrow |9\rangle &: 194 \text{ meV}\\ |1\rangle \rightarrow |7\rangle &: 162 \text{ meV}\\ |1\rangle \rightarrow |6\rangle &: 136 \text{ meV}\\ |1\rangle \rightarrow |5\rangle &: 110 \text{ meV}.\end{aligned}$$

We attribute the four largest peaks to the same transitions as those implied by the experimental group, with an average energy difference of about 10 meV when comparing with the experiment. Comparing the absorption spectrum at $T = 50$ K (figure 26(a)) and 300 K (figure 26(b)), we see that the transition $|1\rangle \rightarrow |5\rangle$ gets relatively weaker with temperature, while the transition $|2\rangle \rightarrow |9\rangle$ get relatively stronger.

The peak in figure 26(b) at 68 meV is not within the range for the measurements by the experimental group. This could be attributed to several transitions with energies close to 68 meV. So can the peak at 42 meV. (In the experiment, there is also a strong peak present at 87.3 meV. This is explained by the experimental group by multi-phonon absorption, and they do not take it into account since it would not contribute to the detection current. This peak is not observed in the simulations.)

12.4 Dependence of the response current on applied ac. field strength

In theory, the response current should be proportional to the square of the applied field strength, $I \propto |F|^2$. In order to test whether the program satisfies this relation, the current responses for different strengths of the applied AC field are shown in figure 27(a). In figure 27(b) we examine the maximum of the current response, $j_{\max}(1)$, as a function of the applied light field strength, and compare it to the relation $y(x) = j_{\max}(1) \cdot x^2$. The data fits very well with the quadratic relation, so the program confirms the theoretical result.

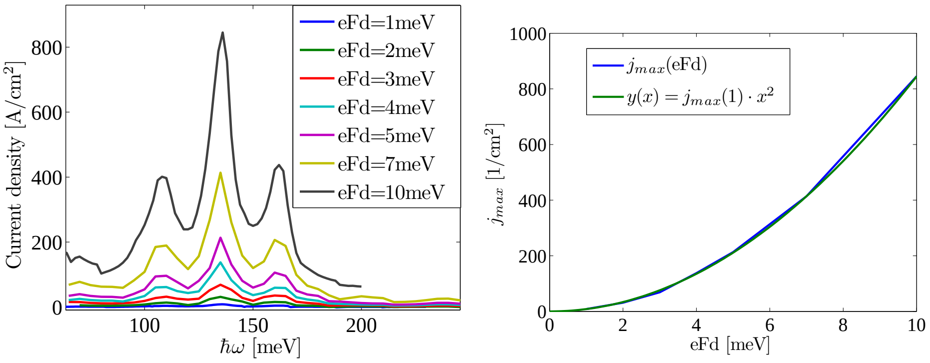

(a) (b)

Figure 27: (a) Current response for different AC field strengths and (b) the maximum value of the response in (a) as a function of applied field strength. The green curve shows a simple quadratic function $y(x) = j_{\max} \cdot x^2$, where $j_{\max}$ is the maximum of the response current taken at $eFd = 1$ meV.

13 Gendron Quantum Cascade Detector, Sample B[4]

13.1 The structure

This sample, call it Sample B, is an improvement of Sample A previously described in section 12, and so is very similar to that one. Sample A had all the barriers the same width, which turned out not to be optimal since it detected at several different frequencies. This sample has the barrier widths tailored in order to minimise the overlap with other excited states than the one preferred for detection.

The heterostructure is shown in figure 28(a). The barriers here are made of $Al_{0.33}Ga_{0.67}As$. The structure is (starting with the ground state well)

$$\underline{68}/\mathbf{56.5}/20/\mathbf{39.55}/23/\mathbf{31}/28/\mathbf{31}/34/\mathbf{31}/38/\mathbf{31}/48\ \text{Å}.$$

It is clear from figure 28(a) that there is only one significant overlap for the excited states with the ground state $|1\rangle$, namely states $|8\rangle$. We would therefore expect much more distinct absorption and response spectra with only one peak.

A remark should be made about the Wannier states calculated for this structure. As described in section 4, the Wannier states are the solutions to the Bloch equation considering only the conduction band potential. The energy of the states would change when considering the mean field and scattering effects, and thus the energy of the states in figure 28(a) will not match the actual transition energies. For the QCL:s we usually plot the Wannier-Stark states, since these do take the

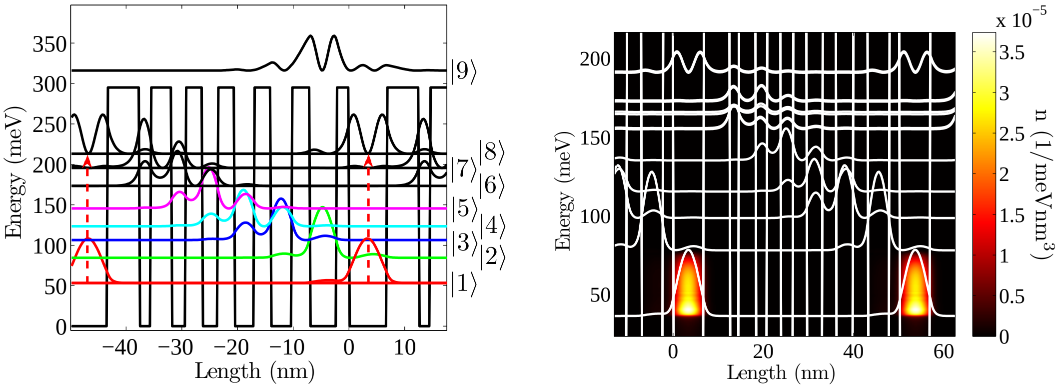

(a)

(b)

Figure 28: (a) Band structure of the [3] Sample B with the resulting Wannier states. The arrow indicates the detection transition. (b) The maxima of the spectral function (proportional to the density of states) in the z-direction as well as the electron density. Here, $T = 50$ K.

above mentioned effects into account, but they cannot be calculated at zero bias, for the reasons discussed in section 4.3. We can plot the spectral function, which is proportional to the density of states, along the z-direction at the energy where it is has a maximum in order to see more accurately where the states are. This is done in figure 28(b), together with the carrier density.

As an example of this issue, the state $|9\rangle$ in figure 28(a) will be lowered enough to come down under the barrier potential (not seen in figure 28(b)), and it will contribute to the absorption spectrum. State $|8\rangle$, active in the detection, is shifted from ~ 210 meV in figure 28(a) to ~ 190 meV in figure 28(b).

13.2 Absorption and response

The gain and response at 50 K is shown in figure 29(a). At 25 K the gain and response does not differ noticeably. Compared to the gain for Sample A (figure 26), there is now only one big peak centred at around 160 meV, as well as some small bumps at around 70, 120 and 226 meV.

With the aid of figures 28(a) and 28(b) we can identify which transitions the absorption and response peaks correspond to. The main peak clearly comes from the transition $|1\rangle \rightarrow |8\rangle$, and the $|1\rangle \rightarrow |7\rangle$ transition is also inside this peak. The transition $|1\rangle \rightarrow |6\rangle$ has an energy of about 119 meV, corresponding to the small bump before the main peak. From the second state, the transition 2→6 has an energy of ≈ 77 meV, probably giving the peak at 69 meV. The Wannier states in figure 28(a) also show a continuum state, $|9\rangle$, which make the transition $|1\rangle \rightarrow |9\rangle$ with energy 263 meV possible. This could then correspond to the peak found at

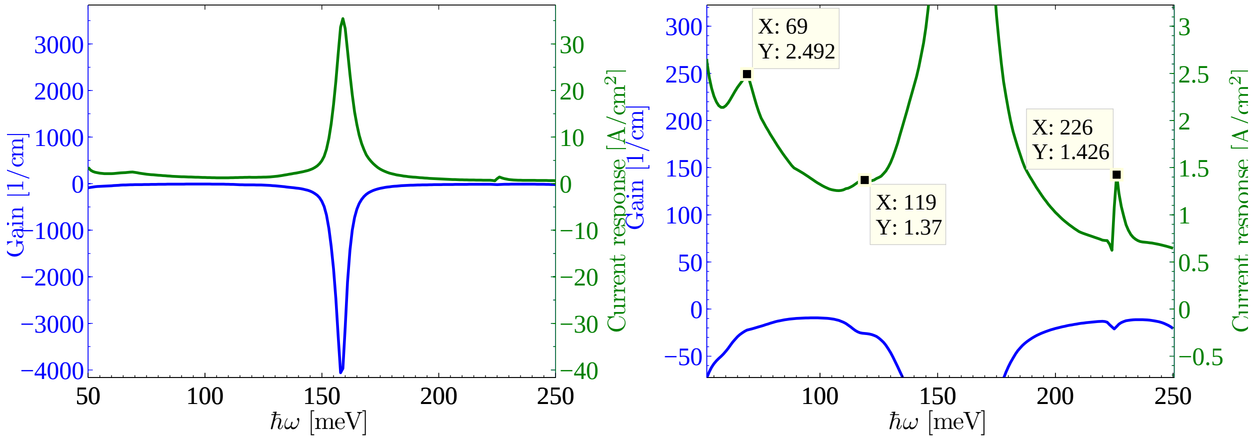

(a) (b)

Figure 29: Gain and response current for $T = 50$ K.

226 meV in figure 29(b).

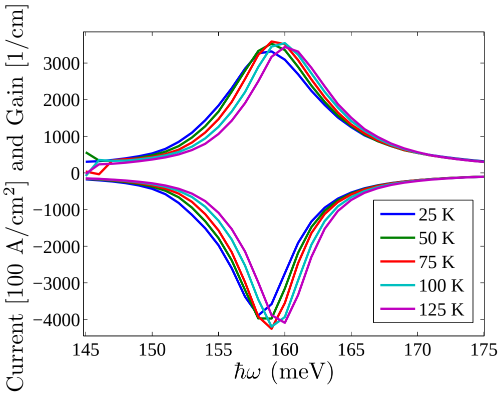

Figure 30: Current (upper curves) and gain (lower curves) for different temperatures. The peak is around 160 meV.

Figure 30 shows the peaks of the spectra for different temperatures. The states have a certain width in energy due to the scattering, and the carriers preferably occupy states with as low energy as possible. The density of states is largest somewhere close to the middle of the energy level, and the electrons will occupy states below this energy for very low temperatures. At higher temperatures, the electrons will start to fill the states with energies closer to the middle of the energy level. For this reason one expects a red-shift with increasing temperature for absorption, contrary to what is shown in figure 30. But if we consider scattering will also increase with temperature, thus broadening the levels even more, we can explain the observed phenomenon by that the electrons are able to occupy even lower states thanks to the additional broadening.

The experimental group found one peak centred at $8\mu\text{m} = 155$ meV and one at $10.3\mu\text{m} = 120$ meV, for the absorption spectrum in figure 31(b). One can see a very small bump in the response measurements in figure 31(a) at $5 - 5.5\mu\text{m}$ corresponding to 225-248 mV. The measurements started at 78 meV, so the peak of lowest energy cannot be seen.

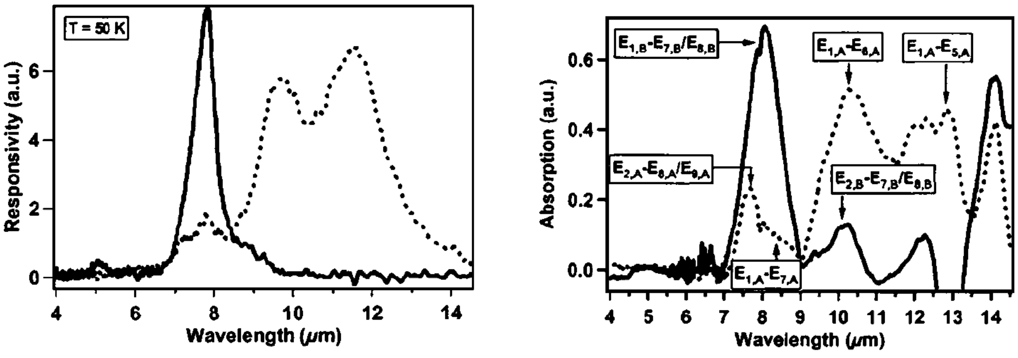

(a)

(b)

Figure 31: (a): Experimentally measured response spectrum at $T = 50$ K. (b): Measured absorption spectrum at $T = 300$K. Both pictures are taken from Ref. [4]. Full lines are for sample B and dashed are for sample A.

In summary the response of Sample B has improved very much compared to Sample A. The main reason is that the higher lying states do not overlap (compare figures 24(a) and 28(a)) as much with the second state, allowing for fewer strong transitions, and that the states are more localised so that they do not overlap with the ground state in the first well. The simulations and experiment have a nice qualitative agreement, but since the group only presented their findings in arbitrary units a quantitative comparison is difficult. We found peaks at nearly the same energies, and attributed them to the same transitions.

13.3 Current simulations

The largest benefit of using a QCD instead of a QWIP is that no applied bias is required for operation, and therefore no dark currents arise that bring noise to the spectrum. There are still some carriers being thermally excited between states in the QCD, which gives some noise. This can be reduced by applying a small backward bias, since the electrons that are excited are less likely to tunnel forward, but instead waits in place until they fall back to the ground state. This is demonstrated in measurements and simulations in Ref. [23], where leakage and noise currents were examined as functions of small applied biases. Simulations and measurements for this structure have been done for small biases, see figure 32, to estimate it's effect on the noise current. We see that at 0 bias, the dark current is larger than at a small backward bias, whereas it increases for forward biases.

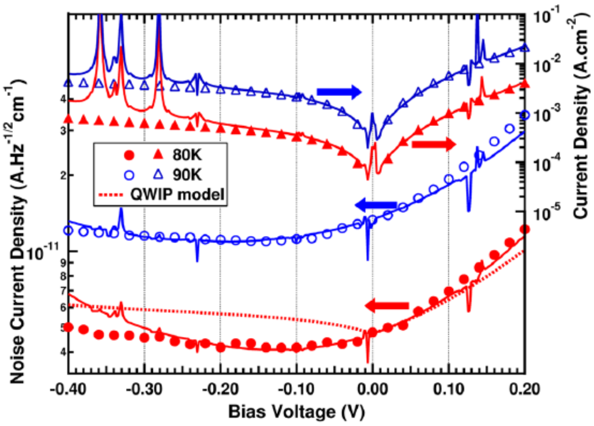

Figure 32: Top (right): Measured and simulated dark current vs. applied bias for the Gendron Sample B QCD. Bottom (left): Dark noise current vs. applied bias. Full lines are theory and markers are experiment. The figure is taken from Ref. [23]. For further details, please refer to this source.

In order to see whether our model can reproduce this result, which would be of use when simulating and improving detectors, an attempt was made to simulate currents for small applied biases, a task that turned out not to be so easy as first expected. It was difficult to get the simulations to converge, apparently because the current is so small. For the same reason the results eventually produced showed features not present in the actual measurements.

The current in figure 33(a) is calculated by reducing the convergence tolerances very far, increasing the number of periods used in the calculations (usually 3, but in this case 5), as well as using data from previous calculations to get good starting values for the iteration process. The size of the currents look reasonable compared to experiment where it is lowest. However, we see regular peaks in the current separated by $\approx$ 7 meV. The Wannier-Stark states are plotted at one such peak at 30 mV/period in figure 33(b). The peaks occur where states from one period aligns with other states from a neighbouring period, giving tunnelling currents over an entire period. The states overlap only to an extremely small extent over this range, but nevertheless the current increases substantially. In the case of figure 33(b), there are alignments of the states $|2\rangle$ of the first period and $|1'\rangle$ of the second period, $|4\rangle$ and $|2'\rangle$, $|5\rangle$ and $|3'\rangle$ as well as $|8\rangle$ and $|6'\rangle$.

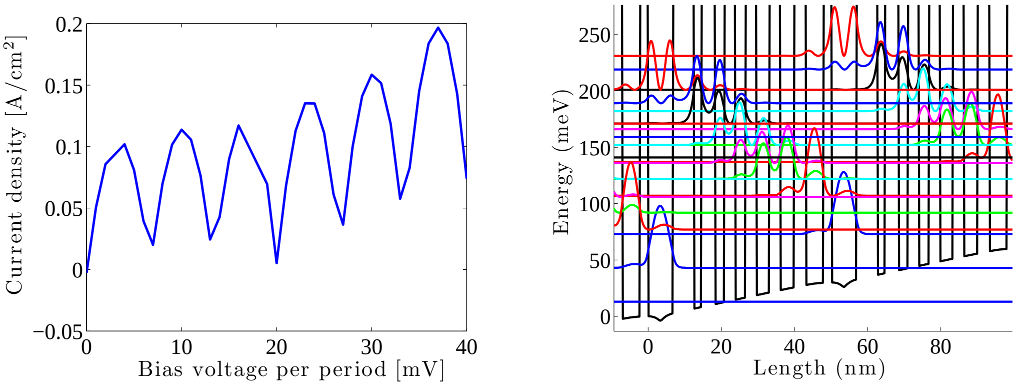

(a)

Figure 33: (a) Current vs. backward bias for $T = 80$ K. (b) Wannier-Stark states at a backward bias of 30 mV per period where the current is peaked. Here $T = 80$ K.

Part III

Conclusions and Outlook

14 Conclusions

In this work THz quantum cascade lasers (QCL) and IR quantum cascade detectors (QCD) have been simulated and analysed. Together with a research team in Canada an article was published in the Journal of Applied Physics [1]. In the article, we describe a "phonon-photon-phonon" design, which look promising, but still has room for improvement.

During the course of this thesis, new QCL structures have continuously been produced by the experimental team in Canada and examined by our team in Lund, leading to new promising QCL structures. The sample by Ghasem Razavipour in section 11 was optimised to give about twice the gain, by tuning the extraction barrier to an appropriate width where the extraction states come into resonance. Here, the effects of and conditions for resonant tunnelling were examined.

The effects of electron-electron scattering in operation has been studied in section 9. The effects are also discussed to some extent in section 10. The lack of scattering induces a lack of thermalisation of the electrons, making it possible for them to tunnel through undesired channels. This has been seen to increase the overall gain, as well as produce pronounced peaks in the current vs. bias curves at biases where states in different wells align. For the V843 structure in section 10 these peaks were also seen in the experiment. The lack of electron-electron scattering is probably the greatest draw-back of the model.

Reality checks of the program (section 12.4) compared to experimental data (sections 10, 12 and 13) have tested the computer program for NEGFT simulations of heterostructure reliable for most structures, in particular those where carrier thermalisation is not so significant. For the QCD:s, the program proved to have difficulties calculating low currents at low biases, but gave an overall accurate result for the response and absorption spectra.

A new way to display the properties of quantum cascade structures in operation has been presented in sections 12 and 13, namely showing the energy maxima of the spectral function. The spectral function is related to the density of states, and at the same time it gives the proper energies of the quantum mechanical states, as well as the approximate shapes of the states. For QCL:s, this is convenient since the basis states are not calculated exactly and might not represent well the interesting features of the system. For QCD:s, the Wannier-Stark states are not defined and the Wannier states are too in-exact. Simply solving the Schrödinger equation would give the mini-band structure coming from the periodicity of the system, which is not so interesting for an analysis of the operating conditions.

15 Outlook

Electron-electron scattering

For future, more accurate and reliable simulations of QCL:s, in particular for structures highly dependent upon or limited by carrier thermalisation, inclusion of electron-electron scattering would be highly beneficial. Adding an interaction term for the electrons is rather difficult, however, and straight forward approaches might consume large amounts of computation time. In order to have an accurate, yet practical, implementation of this many approximations would still have to be used. The scattering would have to be treated with self-energies, just as the phonon scattering terms. One approach that is presently pursued is the GW approximation. This could be a viable solution, although not enough progress has been reach so far to be certain. Successfully implementing electron-electron scattering would be the next main improvement of the program.

Code optimisation

Further improvements of the program that can be done are optimisation and parallellisation of the code, and an overview of whether it is beneficial to include a full treatment of the acoustic phonon interaction.

Scientific research

The research into THz QCL:s to reach higher operating temperatures and a variety of different laser frequencies, is still an active research area. Together with the groups collaborated with in this work, as well as other experimental groups, more structures should be analysed to expose their potentials and how they can be exploited, or their limitations and how they can be avoided. Some structures in this work have been manufactured that do not perform as well as expected, and a deeper analysis of why this is the case can imply what improvements can be done to optimise the structures. I expect there to be many more such structures in the literature. Analysing and optimising existing structures might also be a way to reach the desired operating temperature. There are of course other aspects that could be further improved as well, like the power output, reducing internal losses etc.

Regarding quantum cascade detectors, this thesis was set out to simulate a structure combining a laser and detector in the infra-red, designed to lase at a certain bias, and then detect at zero bias at the same wavelength. This is a very interesting device since it combines the two parts needed for almost any application of infra-red quantum cascade lasers. It would be interesting to simulate these kind of structures if there would be an interest from experimentalists to manufacture such devices.

Several well-controlled QCD:s have been developed, but improvements can still be done on the following points[7]. Quantum efficiency: this is the rate of electrons contributing to the photo-current to the incoming photon flux; Reduction of dark-currents: although the QCD is already much better on this point than the conventional QWIP, it could be reduced further by reducing the transition matrix elements of states other than those responsible to the desired transition; Reducing the detection width: the QCD would be much more useful in practise if the width of the detection spectrum was reduced to tighter match a specific wavelength.

In addition to this there is also a field of THz quantum cascade detectors that would be interesting to explored, since most of the applications for THz QCL depend on THz detection of some kind.

Part IV

Appendix

A Tables with structure data

The tables that follow contain the material parameters used in the simulations of the respective structures. x is the relation of Al to Ga in the $\mathrm{Al}_x\mathrm{Ga}_{1-x}\mathrm{As}$ alloy, and CBO is the resulting conduction band offset to GaAs. V_{AS} is the alloy scattering potential of AlGaAs, a way to somewhat artificially take into account the fact that we are using Bloch functions even though AlGaAs is not a perfect crystal. The sheet doping density n_{dope} is situated in the layer designated with an underline. The interface roughness is characterised by two parameters; λ is the typical width of an island, and ν is the typical distance it penetrates across the interface. These values are not known, rather guesses are made based upon earlier simulations and the atomic radii. Finally, the number of periods N_{per} is given. This depends on a number of things; for QCD:s, for small biases the dark current density is inversely proportional to N_{per}, whereas the responsitivity goes down for larger N_{per}[7]. For QCL:s, larger N_{per} gives larger gain since more photons are emitted, but at the same time the losses increase.

Table 1: Scalari QCL

Parameter	Value	Description
x	0.25	In $\mathrm{Al}_x\mathrm{Ga}_{1-x}\mathrm{As}$
CBO	217.5 meV	Conduction band offset between GaAs/AlGaAs
m_{barr}	$8.775 \cdot 10^{-2}$	Barrier effective mass
V_{AS}	0.1275	Alloy scattering potential of AlGaAs
n_{dope}	$3.25 \cdot 10^{10}\ \mathrm{cm}^{-2}$	Sheet doping density
λ	10 nm	Average roughness distance
ν	0.2 nm	Effective roughness height
N_{per}	276	Number of periods (not used in simulations)

Table 2: V843

Parameter	Value	Description
x	0.25	In $\mathrm{Al}_x\mathrm{Ga}_{1-x}\mathrm{As}$
CBO	217.5 meV	Conduction band offset between GaAs/AlGaAs
m_{barr}	$8.775 \cdot 10^{-2}$	Barrier effective mass
V_{AS}	0.1875	Alloy scattering potential of AlGaAs
n_{dope}	$3.25 \cdot 10^{10}$ cm^{-2}	Sheet doping density
λ	10 nm	Average roughness distance
ν	0.2 nm	Effective roughness height
N_{per}	276	Number of periods (not used in simulations)

Table 3: QCL by G. Razavipour

Parameter	Value	Description
x	0.25	In $\mathrm{Al}_x\mathrm{Ga}_{1-x}\mathrm{As}$
CBO	217.5 meV	Conduction band offset between GaAs/AlGaAs
m_{barr}	$8.775 \cdot 10^{-2}$	Barrier effective mass
V_{AS}	0.1875 meV	Alloy scattering potential of AlGaAs
n_{dope}	$3.25 \cdot 10^{10}$ cm^{-2}	Sheet doping density
λ	10 nm	Average roughness distance
ν	0.2 nm	Effective roughness height
N_{per}	221	Number of periods (not used in simulations)

Table 4: Gendron QCD, Sample A

Parameter	Value	Description
x	0.34	In $\mathrm{Al}_x\mathrm{Ga}_{1-x}\mathrm{As}$
CBO	275 meV	Conduction band offset between GaAs/AlGaAs
m_{barr}	$9.52 \cdot 10^{-2}$	Barrier effective mass
V_{AS}	0.2244	Alloy scattering potential of AlGaAs
n_{dope}	$5 \cdot 10^{11}$ cm^{-2}	Sheet doping density
λ	10 nm	Average roughness distance
ν	0.1 nm	Effective roughness height
N_{per}	10	Number of periods (not used in simulations)

Table 5: Gendron QCD, Sample B

Parameter	Value	Description
x	0.33	In $\mathrm{Al}_x\mathrm{Ga}_{1-x}\mathrm{As}$
CBO	217.5 meV	Conduction band offset between GaAs/AlGaAs
m_{barr}	$8.775 \cdot 10^{-2}$	Barrier effective mass
V_{AS}	0.2211	Alloy scattering potential of AlGaAs
n_{dope}	$3.25 \cdot 10^{10}$ cm^{-2}	Sheet doping density
λ	10 nm	Average roughness distance
ν	0.2 nm	Effective roughness height
N_{per}	276	Number of periods (not used in simulations)

References

[1] E. Dupont, S. Fathololoumi, Z. Wasilewski, G. Aers, S. R. Laframboise, M. Lindskog, A. Wacker, D. Ban, and H. C. Liu: *A phonon scattering assisted injection and extraction based terahertz quantum cascade laser*, J. Appl. Phys. **111**, 073111 (2012).

[2] G. Scalari, M. Amanti, C. Walther, R.Terazxi, M. Beck, and J. Faist: *Broadband THz lasing from a photon-phonon quantum cascade laser*, Optics Express **18**, 8043 (2010).

[3] L. Gendron, M. Carras, A. Huynh, V. Oritz, C. Koeniguer, and V. Berger: *Quantum cascade photodetector*, Applied Physics Letter **85**, 2824 (2004).

[4] L. Gendron, C. Koeniguer, V. Berger, and X. Marcadet: *High resistance narrow band quantum cascade photodetectors*, Applied Physics Letter **86**, 121116 (2005).

[5] B. S. Williams: *Terrahertz quantum-cascade lasers*, Nature photonics **1**, 517 (2007).

[6] T. Commissariat: *Portable lasers probe oil-rig waste*, physicsworld.org (2011).

[7] A. Gomez, M. Carras, A. Nedelcu, E. Costard, X. Marcadet, and V. Berger: *Advantages of quantum cascade detectors*, Proc. SPIE **6900**, 69000J (2008).

[8] J. Faist *et al.*: *Quantum cascade laser*, Science **261**, 553 (1994).

[9] R. Koehler, A. Tredicucci, F. Beltram, H. E. Beere, E. H. Linfeld, A. G. Davies, D. A. Ritchie, R. C. Iotti, and F. Rossi: *Terahertz semiconductor heterostructure laser*, Nature **417**, 156 (2002).

[10] S. Fathololoumi, E. Dupont, C. Chan, Z. Wasilewski, S. Laframboise, D. Ban, A. Mátyás, C. Jirauschek, Q. Hu, , and H. C. Liu: *Terahertz quantum cascade lasers operating up to $\sim$ 200 k with optimized oscillator strength and improved injection tunneling*, Opt. Express **20**, 3866 (2012).

[11] A. Wacker: *Quantum Cascade Laser: An Emerging Technology in Nonlinear Laser Dynamics* (Wiley-VCH, Berlin, 2011).

[12] A. Wacker: *Semiconductor superlattices: A model system for nonlinear transport*, Physics Report **357**, 1 (2002).

[13] H. Haug and A.-P. Jauho: *Quantum kinetics in transport and optics of semiconductors* (Springer, 1996).

[14] A. L. Fetter and J. D. Walecka: *Quantum theory of many-particle systems* (McGraw Hill, Inc, 1971).

[15] C. Sirtori, P. Kruck, S. Barbieri, P. Collot, J. Nagle, M. Beck, J. Faist, and U. Oesterle: *$GaAs/Al_xGa_{1-x}As$ quantum cascade lasers*, Applied Physics Letters **73**, 3486 (1998).

[16] T. Brandes: *Truncation method for green's functions in time-dependent fields*, Physical Review Letters B **56**, 1213 (1997).

[17] P. Y. Yu and M. Cardona: *Fundamentals of semiconductors* (Springer, 1999).

[18] A. Wacker: *Coherence and spatial resolution of transport in quantum cascade lasers*, physica status solidi (c) **5** (2008).

[19] J. D. Jackson: *Classical Electrodynamics third edition* (John Wiley sons inc., 1999).

[20] D. Burghoff, T.-Y. Kao, D. Ban, A. W. M. Lee, Q. Hu, and J. Reno: *A terahertz pulse emitter monolithically integrated with a quantum cascade laser*, Appl. Phys. Lett. (2011).

[21] H. Callebaut and Q. Hu: *Importance of coherence for electron transport in terahertz quantum cascade lasers*, J. Appl. Phys. **98**, 104505 (2005).

[22] H. Li, J. C. Cao, J. T. Lü, and Y. J. Han: *Monte carlo simulation of extraction barrier width effects on terahertz quantum cascade lasers*, Appl. Phys. Lett. **92**, 221105 (2008).

[23] A. Delga, M. Carras, L. Doyennette, V. Trinite, A. Nedelcu, *et al.*: *Predictive circuit model for noise in quantum cascade detectors*, Appl. Phys. Lett. **99**, 252106 (2011).